

Detecting contact areas in vibrating steel beams using Energy Flux

M.H. van Dijk

Technische Universiteit Delft

Detecting contact areas in vibrating steel beams using Energy Flux

by

M.H. van Dijk

to obtain the degree of Master of Science
at the Delft University of Technology,
to be defended publicly on January 28th: 13:30 - 15:00

Student number: 4245652
Project duration: December, 2019 – January, 2021
Thesis committee: Prof. Dr. A.V. Metrikine, TU Delft, daily supervisor
MSc V. Vaniushkina, TU Delft, supervisor
Dr. Ir. S. Sánchez Gómez, TU Delft, supervisor
Ir. T. Kamphuis, DOT, external supervisor

An electronic version of this thesis is available at <http://repository.tudelft.nl/>

*If you want to find
the secrets of the universe,
think in terms of
energy, frequency and vibration.*

NIKOLA TESLA

ABSTRACT

The world faces an increasing energy problem, forcing people to search for sustainable energy sources. Off-shore wind energy has shown great potential to financially compete with traditional energy sources. Recent developments like the slip-joint connection increase this potential. However, for further optimization of the design of a slip-joint, the location of the contact areas between the two cones must be known. Previous attempts to detect these contact areas based on techniques such as heat transfer or ultrasonic measurements have proven insufficient. A possible new way of detecting contact areas, is through the behaviour of Energy Flux. Energy Flux methods have shown great potential as a damping identification tool in other applications. Therefore, in this study the relation between Energy Flux behaviour and the presence of a contact point in the time-, frequency- and time-frequency-domain is studied. To this end, a numerical analysis of a vibrating simply supported Euler Bernoulli beam is conducted, simulating a contact area with a point load. The analysis in the frequency-domain showed the most promising results. Presence of a contact point (i) introduces peaks at twice the first and twice the second eigenfrequencies, and (ii) increases peak height at the location of the contact point. The pressure of the simulated contact point increased these effects. In the time-domain the presence of a contact point increased the amplitude of the cumulative energy flux. This change was most significant at the antinode of the first eigenmode. The location of the contact point was of little influence on this effect. These results show that the presence of a contact area influences the behaviour of the energy flux. The results are encouraging for a later implementation of the energy flux method for the detection of contact areas in a slip-joint. As a validation of these results, an experiment has been proposed. After execution of this experiment, further research is needed in (i) the behaviour of Energy Flux in a conical shape, and (ii) Energy Flux measurements of higher frequencies.

PREFACE

As I add the final words to my thesis, it seems my time as a student is coming to an end. What a journey it has been. During these past years, I've had so many wonderful opportunities and this preface seems as good a time as any to say a few final *thank-you's*.

First of all, thanks for the amazing guidance I have received during my thesis. It has truly been a pleasure to work with a few of the brightest minds of the world. Sergio, even though you joined the committee later on in the project, you really helped kick-start my thesis with your clear explanation on the theory on Energy Flux. Valentina, my many quick questions at random times must have, at some point or another, been annoying. Therefore I am very grateful that you kept on answering, and were always available to me. DOT, in general for hosting me at the start, and Thijs specifically for his contribution to the project. Thijs, you kept on surprising me with your knowledge, but I am most grateful that you always kept my interests at heart, and made sure I did as well. This has truly improved my last months as a student. And lastly, prof Metrikine, the entire faculty seems to look up to you, and after having worked with you, I completely understand why. Your combination of intellect and understanding/answering questions is one-in-a-million. It has been a pleasure to work with you all.

Secondly, I want to thank all the friends that have made these last few years as amazing as they were. FC Slippertje, LvC, KVZ520, Fakantie, B122 including all PS committees/boards, DSAV '40, Ari9, AnalyseGang, MDP271, and many, many more. I also want to thank my family, Mam, Pap, Tim en Jolijn. You've been with me from the very start, you must have had your doubts at times, but never left my side. Lastly, Sophie, your endless love, support and patience have helped me more than you can imagine. I can't wait to start a this new chapter with you.

M.H. van Dijk
Delft, Thursday 21st January, 2021

NOMENCLATURE

LIST OF ACRONYMS

ADC	Analog-to-Digital Converter
CEF	Cumulative Energy Flux
DOT	Delft Offshore Turbine
EBBT	Euler Bernoulli Beam Theory
EF	Energy Flux
MAV	Mean Absolute Value
PLL	Point Load Location

LIST OF SYMBOLS

Variable	Description	Units
ϵ	Strain	m/m
κ or w''	Curvature	$radian$
λ	Wavelength	m
ρ	Density	kg/m^3
τ	Angle	$degree$
ϕ or w'	Rotation	$degree$
ω_n	Natural angular frequency	rad/s
A	Area	m^2
e	Energy Density	J/m^3
E	Young's Modulus	GPa
E_b	Potential Bending Deformation Energy	J
E_h	Potential Height Energy	J
E_k	Kinetic Energy	J
EI	Bending stiffness	Nm^2
f	Frequency	Hz
G	Shear Modulus	GPa
GA	Shear Stiffness	Nm^2
I	Moment of Inertia	mm^4
K	Kinetic Energy	J
M or w''''	Moment	Nm
P	Potential Energy	J
R	Radius of curvature	m
S	Energy Flux	J/s
V or w'''	Shear Force	N
w	Displacement	m
\dot{w}	Velocity	m/s
\ddot{w}	Acceleration	m/s^2
\dot{w}'	Rotational Velocity	$degree/s$

LIST OF FIGURES

1.1	Rapid growth in offshore wind farm installations in Europe. The offshore capacity is expected to grow further. Acquired from Komušanac (2020).	1
1.2	Typical foundation concepts and their market shares in commercial projects as of 2012. (a) Gravity-based foundation (16%), (b) Monopile foundation (74%), (c) Caisson foundation (0%), (d) Multipile foundation (5%), (e) Multi caisson foundation (0%) and (f) Jacket foundation (5%). Acquired from EWEA (European Wind Energy Association) (2013).	2
1.3	Evolution of the monopile-turbine interface. The slip-joint connection, developed by DOT, offers multiple advantages over the grouted and bolted connection. Acquired from (Kamphuis, 2016a)	2
2.1	Conceptional drawing of a slip-joint connection. The bottom part is connected to the monopile and the upper part to the transition piece. Acquired from Segeren (2017).	5
2.2	The first three eigenmodes, as found in (Spijkers et al., 2005b)	7
2.3	Geometrical relations	9
2.4	Flowchart of calculations	10
3.1	Example setup for the analyses.	11
3.2	ANSYS model for the numerical analysis, with the 3-dimensional representation shown. The actual mesh is 1-dimensional. Supports are present, but not shown in this figure.	13
3.3	Mechanical Model with the measurement locations	14
3.4	The location of point load locations 1, 2, 3 and 4. PLL 1 is located at the midpoint of the beam.	14
4.1	Configuration options for a full bridge strain gauge	16
4.2	Strain configurations to be used in the experiment	17
5.1	Effect of the point load on the shape of the second eigenmode.	20
5.2	Example of Energy Flux in the time-domain	21
5.3	Example of Energy Flux through all locations	21
5.4	Cumulative Energy Flux through three locations, without added weight.	22
5.5	Normalized Energy Flux on all locations, with 2kg at location 8	23
5.6	Cumulative Energy Flux through three locations, without added weight.	23
5.7	Cumulative Energy Flux through location 6, with increasing weight at location 8	24
5.8	Cumulative Energy Flux through location 4 with increasing weight at location 8	24
5.9	Example of a Fourier analysis of Energy Flux through location 7. In this example, no weight was added	25
5.10	Example of a Fourier analysis of Energy Flux through location 7. In this example, no weight was added	26
5.11	The height of the peaks along the length of the beam	26
5.12	The behaviour of all peaks over the length of the beam	27
5.13	Example of a Fourier Analysis of Energy Flux through all locations. With 2kg on PLL 2	27
5.14	Zoomed in example of a Fourier analysis at the location of the weight	28
5.15	Comparison between the amplitudes of the FFT peaks, with and without added weight	29
5.16	Behaviour of the amplitude over the length of the beam, with an increasing weight	29
5.17	Wavelet analyses without any weights	30
5.18	Top view of the experiment set-up	31
6.1	The change in stored energy over time, and the change in Energy Flux over x.	34
6.2	C values for simply supported beams, as found in (Spijkers et al., 2005a)	35
6.3	Global Mode Shapes, as found by (Segeren, 2017)	36

A.1	Cumulative Energy Flux through three locations, without added weight.	40
A.2	Overview of the behaviour areas of the cumulative Energy Flux	40
A.3	The expected results of the experiment with PLL 1.	40
A.4	The expected results of the experiment with PLL 2.	41
A.5	The expected results of the experiment with PLL 3.	41
A.6	The expected results of the experiment with PLL 4.	42
B.1	CEF through all locations with 1 kilogram at PLL 1	43
B.2	CEF through all locations with 2 kilogram at PLL 1	44
B.3	CEF through all locations with 3 kilogram at PLL 1	44
B.4	CEF through all locations with 4 kilogram at PLL 1	45
B.5	CEF through all locations with 5 kilogram at PLL 1	45
B.6	CEF through all locations with 1 kilogram at PLL 2	46
B.7	CEF through all locations with 2 kilogram at PLL 2	46
B.8	CEF through all locations with 3 kilogram at PLL 2	47
B.9	CEF through all locations with 4 kilogram at PLL 2	47
B.10	CEF through all locations with 5 kilogram at PLL 2	48
B.11	CEF through all locations with 1 kilogram at PLL 3	48
B.12	CEF through all locations with 2 kilogram at PLL 3	49
B.13	CEF through all locations with 3 kilogram at PLL 3	49
B.14	CEF through all locations with 4 kilogram at PLL 3	50
B.15	CEF through all locations with 5 kilogram at PLL 3	50
B.16	CEF through all locations with 1 kilogram at PLL 4	51
B.17	CEF through all locations with 2 kilogram at PLL 4	51
B.18	CEF through all locations with 3 kilogram at PLL 4	52
B.19	CEF through all locations with 4 kilogram at PLL 4	52
B.20	CEF through all locations with 5 kilogram at PLL 4	53

LIST OF TABLES

3.1	Properties of the beam	12
3.2	Eigenfrequencies of the beam	12
5.1	Overview of Energy Input for every system, expressed in Joule. PLL refers to the location of the point load. For all locations six magnitudes were studied, ranging from 0 to 5 kilograms.	19
5.2	Eigenfrequencies of the various systems	20
5.3	The increase of mean absolute value of the Energy Flux, at all locations for all point load locations	22
5.4	The location of the last two peaks, for 1 kilogram at each PLL	28
5.5	Influence of the weight on the magnitudes of the peaks in the Fourier analysis of the Energy Flux through location 6.	30
6.1	The calculated analytical eigenfrequencies of the system	35

CONTENTS

List of Figures	ix
List of Tables	xi
1 Introduction	1
1.1 Research Motivation	1
1.2 Current Methods and Limitations.	3
1.3 Research Questions	3
1.4 Outline	3
2 Background and Theory	5
2.1 Slip-joint Connection	5
2.2 Contact Areas	6
2.3 Euler-Bernoulli Beam Theory	6
2.3.1 Assumptions	6
2.3.2 Derivation	7
2.3.3 Structural Vibration	7
2.4 Energy Flux	8
2.4.1 Measuring Energy Flux.	8
2.4.1.1 Moment - M	9
2.4.1.2 Rotational Velocity - \dot{u}'	9
3 Numerical Analysis	11
3.1 Set-up.	11
3.2 Beam properties	12
3.3 Numerical Simulation in ANSYS	12
3.4 ANSYS Model	12
3.4.1 Model Description	12
3.4.1.1 Load Description	14
3.4.1.2 Output Description	14
4 Experimental Approach	15
4.1 Experiment Requisites	15
4.2 Building Blocks of the Experiment	17
5 Results	19
5.1 Numerical Results.	19
5.1.1 Influence of Point Load on System Properties	19
5.1.2 Time-Domain	21
5.1.3 Frequency-Domain	25
5.1.4 Time-Frequency-Domain	30
5.2 Design of Experiment	31
5.2.1 Final Design	31
5.2.2 Expected results of the experiment.	31
5.2.3 Follow up experiments.	32
6 Discussion	33
6.1 Interpretation of the results	33
6.1.1 Time-Domain	33
6.1.2 Frequency-Domain	33
6.2 Difference between the two Energy Flux equations	34
6.3 Validity of the Model	34

6.4	Application in the slip-joint	35
7	Conclusions and Recommendations	37
7.1	Key Findings	37
7.2	Suggestions for Further Research	38
A	Expected Experiment Results	39
B	Cumulative Energy Flux Results	43
B.1	PLL 1	43
B.2	PLL 2	46
B.3	PLL 3	48
B.4	PLL 4	51
	Bibliography	55

1

INTRODUCTION

1.1. RESEARCH MOTIVATION

The global population is rapidly increasing, leading to a growth in energy demand. Nowadays, a serious energy crisis and environmental pollution have forced humankind to look for sustainable alternative sources of energy. Wind and solar energy are the most available sources of renewable energy. Wind power is considered the most promising, because of its low complexity in installation and maintenance and the highest production of overall energy (Yuryevich and Wong, 1999).

For these reasons, wind power has been the fastest growing form of renewable energy over the last years. Renewable energy could contribute 80% of global energy supply by 2050, according to a report from the Intergovernmental Panel on Climate Change (IPCC) (Edenhofer et al., 2011) Wind energy will most likely play a significant role in electricity supply in 2050. The development of offshore wind farms becomes increasingly important, because land availability onshore is restricted (Sun et al., 2012). Figure 1.1 shows the annual onshore and offshore wind installations in Europe from the last ten years. The figure shows that offshore wind energy becomes more and more popular.



Figure 1.1: Rapid growth in offshore wind farm installations in Europe. The offshore capacity is expected to grow further. Acquired from Komušanac (2020).

A wind energy converter consists of a wind turbine installed on top of a support structure and foundation. The support structures and foundations that are currently employed by industry are presented in Figure 1.2. The monopile structure is the most popular foundation concept, because of its cheapness and constructability (Yoon et al., 2014). The installation of a monopile consists of several steps. First of all, a monopile is driven into the seabed. Then a transition piece is put on top of this, followed by the tower, and nacelle and rotor

blades. By reducing both the number of steps, the installation time and weather sensitivity of each step, significant cost savings could be achieved.

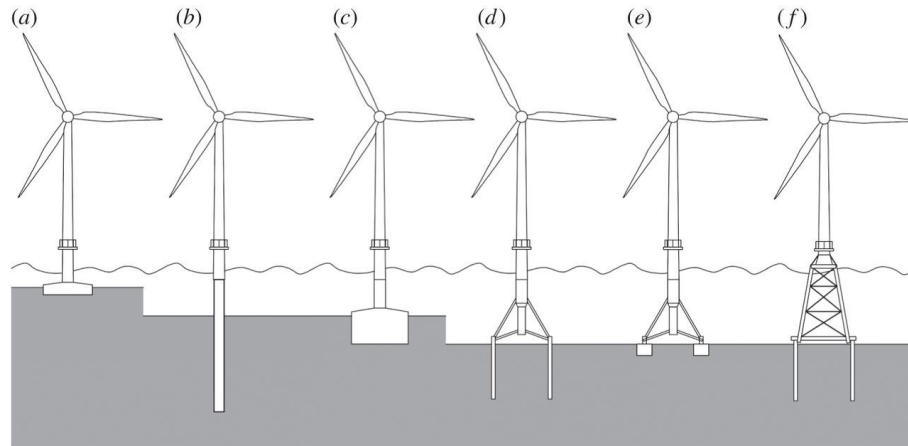


Figure 1.2: Typical foundation concepts and their market shares in commercial projects as of 2012. (a) Gravity-based foundation (16%), (b) Monopile foundation (74%), (c) Caisson foundation (0%), (d) Multipile foundation (5%), (e) Multi caisson foundation (0%) and (f) Jacket foundation (5%). Acquired from [EWEA \(European Wind Energy Association\) \(2013\)](#).

One of the steps that is being improved is the monopile-turbine interface. The most common connection in European offshore wind farm foundations between the monopile and the transition piece is a concrete (grout) connection (Figure 1.3 A). An ultra-high strength grout material is then used to fill in the gap between a transition piece and the monopile. Although grouted connections have been proven successful, the industry has started using bolted connections (Figure 1.3 B). This is a flanged connection, in which the two parts are bolted together. Over the last years, Delft Offshore Turbine (DOT) further developed a new transition piece for the monopile, known as the slip-joint (Figure 1.3 C). The slip-joint is a mechanical, friction-based connection that consists of two conical sections, one attached to the top of the foundation pile and the other to the bottom of the transition piece. Such a slip-joint connection provides many advantages over a grouted or flanged connection. A slip-joint enables higher loads, reduces maintenance costs and enables a rapid installation. However, for the slip-joint to be accurately designed and to have its performance guaranteed, it is necessary to know the contact behaviour within the slip-joint.

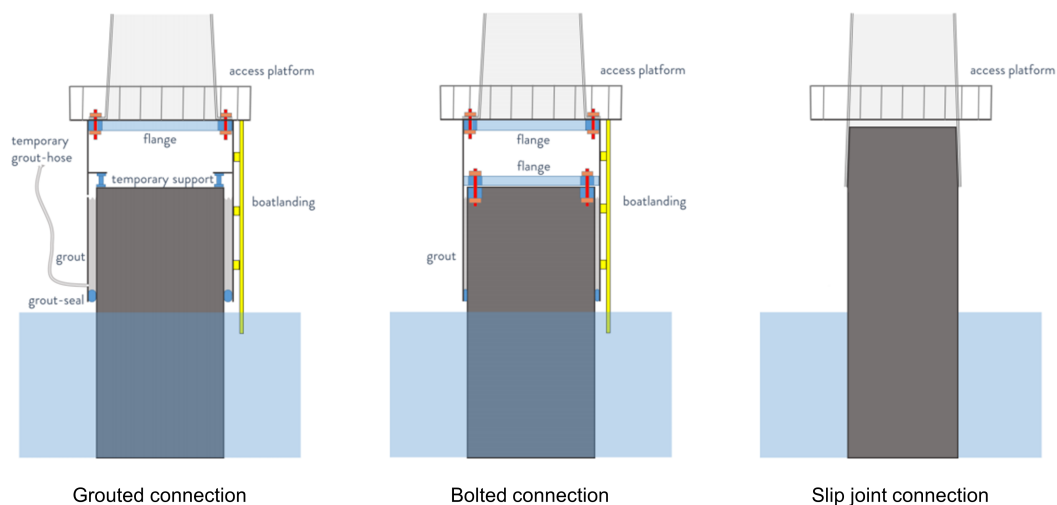


Figure 1.3: Evolution of the monopile-turbine interface. The slip-joint connection, developed by DOT, offers multiple advantages over the grouted and bolted connection. Acquired from [\(Kamphuis, 2016a\)](#)

1.2. CURRENT METHODS AND LIMITATIONS

After the installation of a monopile using a slip-joint connection, it is currently unknown what the stress distribution and contact area within the joint are. Because the behaviour of the contact areas is unknown, the construction has to be over-dimensioned to fulfill safety requirements. Several techniques, like heat transfer (Atkinson, 2018) and ultrasonic measurements (Kamphuis, 2016b), have been used to measure the slip-joint contact area. However, these techniques did not work, or had major drawbacks.

Energy Flux (EF) could be a promising technique to detect contact areas between transition pieces and monopiles on wind turbine foundations. Currently, the Energy Flux method has been successfully used in the identification of damage in connections of high-rise buildings (Sanchez Gomez, 2019).

1.3. RESEARCH QUESTIONS

The analysis of Energy Flux may reveal information about the contact areas between a transition piece and the monopile. The aim of this study is to develop a numerical and experimental methodology that uses Energy Flux to detect contact areas in a simplified wind turbine, represented as a 1D steel beam. To strive for a better understanding of Energy Flux in a vibrating beam, the following research question was formulated:

How can the Energy Flux method be used to detect contact areas in a vibrating steel beam?

To solve this research question, two sub-questions are presented that need to be answered in order to make the main question more transparent.

1. *What is the influence of a contact point on Energy Flux in the time-domain, frequency-domain and time-frequency-domain?*

Based on a numerical model developed in ANSYS, the influence of a contact point on Energy Flux will be simulated. These results will be analyzed in three different domains (time, frequency and time-frequency). Each domain may provide additional information of the effect of a simulated contact area on Energy Flux.

2. *How can the numerical results be validated in an experiment?*

The outcome of the numerical study may reveal an in-depth understanding on the behaviour of Energy Flux with and without contact areas. In order to use Energy Flux in industry, the Energy Flux should be validated in experiments. A step-by-step experiment set-up will be developed in this study.

1.4. OUTLINE

Chapter 2 provides background information that is relevant for the understanding of the processes regarding Energy Flux in a vibrating beam. The main topics in this chapter are theory on the slip-joint connection, the meaning and simulation of a contact area and theory on Energy Flux. In Chapter 3 the methodology, and the implementation of the numerical analysis are covered. The numerical model is described, and the approach of the analysis is explained. The experimental part uses a similar approach and is further discussed in Chapter 4. The most important results regarding the numerical analysis of the Energy Flux and the experiment set-up are presented in Chapter 5. Results of all other analyses can be found in Appendix A. Subsequently, the main topics of discussion that concern implications on the presented results and points for improvement will be discussed in Chapter 6. In conclusion, Chapter 7 will present brief answers to the research questions and provide recommendations for further research.

2

BACKGROUND AND THEORY

2.1. SLIP-JOINT CONNECTION

A major challenge in offshore wind technology is transferring loads from the upper tower to the foundation of the structure. The *transition piece* is a critical component, which is designed to resist bending moments, shear stresses and axial loads coming from wave, wind and current loads (Lee et al., 2016). Traditionally, a transition piece is executed using a grouted connection. This connection had been widely used in the oil and gas industry and with satisfactory performance (Lotsberg, 2013, e.g). For this reason, the grouted connections were thought to be sufficiently strong for offshore wind turbines. However, in 2009, it was observed that the grouted connections at the offshore wind turbines of Egmond aan Zee were settling (Segeren et al., 2014). Later on, also implications of several other wind farms indicate that the strength of the grouted connections was inadequate (Tziavos et al., 2016). Lotsberg et al. (2012) showed that loads in offshore wind turbines are significantly different than those in marine structures. Hence, a new solution for fitting a transition piece onto an installed monopile was required to endure environmental forces.

To circumvent these problems, a *slip-joint connection* was proposed. This was firstly done by a company called WindMaster. In the 1990s, they used this innovative connection in its onshore turbines. The company went bankrupt in 1998 and the idea fell into desuetude (Segeren, 2017). A few years later, Van der Tempel and Lutje Schipholt (2003) studied whether slip-joint connections could be used for offshore wind turbines. The results of their study were very promising and showed a reduction of installation time and overall costs, compared to traditional grouted connections. Even though the results of the study were very favourable, slip-joints were not used in the industry yet (Segeren, 2017). The Dutch company Delft Offshore Turbine (DOT) further studied the possibilities of using slip-joint connections for offshore wind turbines. In 2016 an onshore turbine was built within the DOT500 project. In 2018, the first offshore wind turbine using the slip-joint connections were successfully installed off the coast of IJmuiden (Topsector Wind, 2018).

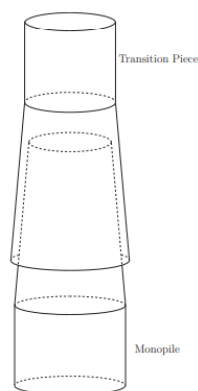


Figure 2.1: Conceptual drawing of a slip-joint connection. The bottom part is connected to the monopile and the upper part to the transition piece. Acquired from Segeren (2017).

The principle of the slip-joint connection basically consists of two cups that fit together, as illustrated in Figure 2.1. The lowest cup is connected to the monopile and the upper cup to the transition piece. Frictional forces between the contact surfaces result in stability and load transfer (Segeren, 2017).

According to Segeren (2017), the slip-joint connection presents a number of advantages compared to grouted connections. The advantages are listed below:

1. Reduction of steel and grout;
2. The possibility of dividing the monopile foundation into two or more sections;
3. Faster installation of the transition piece;
4. Prevention of progressive settlement;
5. Decommissioning of the joint.

However, there also are some challenges that arise in the design, installation, and operational phase of the connection. In this study, the focus is on the *effective contact areas* between the surfaces of the cones. Reduced contact areas, lead to higher stresses which will affect the lifetime. Currently, the location and sizes of the contact areas are unknown. A minimal amount of contact areas is assumed and the slip-joint connections are executed larger than is probably required. When the effective contact areas would be known, material could be reduced. In this study, the Energy Flux method is used to analyse the cones' contact areas.

2.2. CONTACT AREAS

The main goal of this study is to analyse the surface contact between the monopile and the transition piece. The contact that is achieved between the two cones is achieved from the imperfections of the surfaces. These imperfections are a result from manufacturing tolerances and the installation process (Segeren, 2017). Reduced contact areas lead to higher stress, which might result in a limiting lifetime. Therefore, it is important to know the location of the contact areas.

A contact area consists of a force, distributed over a certain size area. This contact force is often decomposed into an orthogonal and a normal component. The normal component being perpendicular to the surface area and the orthogonal component being parallel to the surface area. To model a contact area in an experiment, a weight could be used. This weight will distribute its own weight, over the area of contact. Numerically, a contact area can be modeled by a point load in a 1-dimensional model, and a pressure area in a 2-dimensional model.

2.3. EULER-BERNOULLI BEAM THEORY

In the theory about vibration of systems, a distinction is made between *discrete* and *continuous* systems. Discrete systems have a finite number of degrees of freedom. The vibration of discrete systems can be described by a set of ordinary differential equations. Structural components like beams on the other hand, are considered as continuous systems. These systems have an infinite number of degrees of freedom. The vibration of continuous systems is described by partial differential equations, which involve variables that depend on time and space (Shabana and Ling, 1997).

Several theories exist that analyses the structural vibration of beams, simply referred to as "beam theories". A beam theory provides a relatively simple tool to analyze a beam. There are also more complex tools available, such as the finite element method, to analyze stresses in structures. However, beam theories are still often used, because they provide valuable information about the behaviour of continuous systems (Bauchau and Craig, 2009). One of the most popular beam theories is the *Euler-Bernoulli beam theory*.

2.3.1. ASSUMPTIONS

EBBT describes the relation between the deflection of a beam and an applied load. The theory is widely applied on beams with small deflections under lateral loads only. A fundamental assumption of the Euler-Bernoulli beam theory states that the plane cross-sections remain plane and perpendicular to the neutral axis after bending (Graff, 2012, Rao, 1995). This means that no deformations occur in the cross-section of the beam, since an infinitely rigid cross-section is assumed (Bauchau and Craig, 2009). This is the case in bending deformations, but not in shear deformation. Shear deformation is therefore not taken into account.

This also means that if the neutral axis is located in the middle of the beam, the strains on top of the beam, are equal and opposite to the strains on the bottom of the beam. Another assumption EBBT makes, is that the deformed beam slopes are small. Meaning that if we let $\phi = \frac{dw}{dx}$, this assumption lets $\phi^2 = 0$, as ϕ is assumed very small.

2.3.2. DERIVATION

The listed advantages of section 2.3.1 result in the following equation:

$$\frac{d^2 w}{dx^2} = \frac{M}{EI} \quad (2.1)$$

in which EI is the bending stiffness, M is the moment and $\frac{d^2 w}{dx^2}$ is the second derivative of the deflection. The bending stiffness is a property of the beam shape and material, and can easily be calculated. E is given by the young's modulus of steel, and I can be calculated using $I = \frac{1}{12}bh^3$. This now describes the behaviour of the beams deflection, under a lateral load.

2.3.3. STRUCTURAL VIBRATION

Free vibration is the natural response of a system to any temporary given force or displacement. This response depends on the properties of the system, and is therefore well suited for the detection of small variations within the system. For this thesis, free vibration was examined. The behaviour of an Euler Bernoulli beam in free vibration is shortly discussed here.

Free vibration is governed by a homogeneous partial differential, see equation 2.2. The solution is given by equation 2.3, whose parameters depend on the boundary conditions of the system. For a simply supported beam, this results in equation 2.4. In this solution, n refers to the eigenmode of the system. These eigenmodes are illustrated in figure 2.2. The corresponding eigenfrequencies can be calculated using equation 2.5 (Spijkers et al., 2005b).

$$EI \frac{\partial^4 w(x, t)}{\partial x^4} + \rho A \frac{\partial^2 w(x, t)}{\partial t^2} = 0 \quad (2.2)$$

$$w(x) = A \cosh(\beta x) + B \sinh(\beta x) + C \cos(\beta x) + D \sin(\beta x) \quad (2.3)$$

$$w_n(x) = D_n \sin\left(n\pi \frac{x}{l}\right) \quad (n = 1, 2, \dots, \infty) \quad (2.4)$$

$$\omega_n = C \cdot \sqrt{\frac{EI}{\rho AL^4}} \quad (2.5)$$

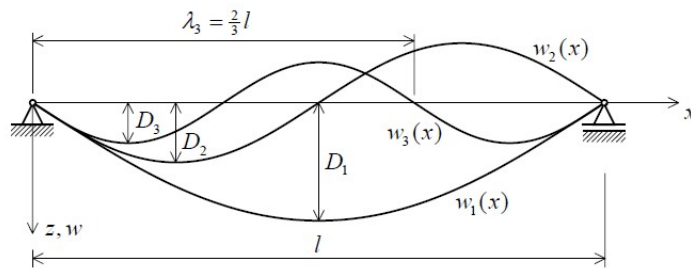


Figure 2.2: The first three eigenmodes, as found in (Spijkers et al., 2005b)

2.4. ENERGY FLUX

There are two ways energy can be stored in a vibrating Euler-Bernoulli beam. Potential energy through deformation and kinetic energy through movement. Multiple theories exist on the kinds of deformation that is relevant. This derivation follows Euler-Bernoulli Beam Theory (EBBT). That means that the only relevant deformation is bending deformation, meaning shear deformations will not be taken into account. The quantities can be calculated using the formulas 2.6 for the potential, and 2.7 for the kinetic energy.

$$P = \frac{1}{2} \int EI \left(\frac{d^2 w}{dx^2} \right)^2 dx \quad (2.6)$$

$$K = \frac{1}{2} \int \rho A \left(\frac{dw}{dt} \right)^2 dx \quad (2.7)$$

This means that if we only consider a small part of the beam, we can calculate the stored energy. This is known as the energy density. This energy density can be rewritten using the equation of motion (equation 2.9), and describes over time, given in equation 2.10

$$e = EIw'' + \rho A \dot{w} \quad (2.8)$$

$$EI \frac{d^4 w}{dx^4} = -\rho A \frac{d^2 w}{dt^2} = 0 \quad (2.9)$$

$$\frac{\partial e}{\partial t} = EIw'' \dot{w}'' - EIw'''' \dot{w} \quad (2.10)$$

The energy variation law states that, in a non dissipating system equation 2.11 applies. This gives us an expression for $\frac{\partial S}{\partial x}$.

$$\frac{\partial e}{\partial t} = -\frac{\partial S}{\partial x} \quad (2.11)$$

$$\frac{\partial S}{\partial x} = -EIw'' \dot{w}'' + EIw'''' \dot{w} \quad (2.12)$$

After integration, this gives the equation of Energy Flux in an Euler Bernoulli beam.

$$S = -EIw'' \dot{w}' + EIw'''' \dot{w} \quad (2.13)$$

This concludes the derivation of Energy Flux in an Euler-Bernoulli beam. However, not all quantities are known at every section of the beam, so measuring Energy Flux brings its difficulties.

2.4.1. MEASURING ENERGY FLUX

When integrated over time, Energy Flux in a semi-infinite beam has another can be written as:

$$S = -M \cdot \dot{w}' + V \cdot \dot{w} = 2 \cdot M \cdot \dot{w}' \quad (2.14)$$

in which M is the moment, V is the shear force and w is the transverse displacement. Also, $\dot{w} = \frac{\partial w}{\partial t}$ and $w' = \frac{\partial w}{\partial x}$. Since in an existing structure, it is difficult to measure shear force, the latter equation will possibly be used for the measurements in the experiment. From equation 2.14 we can see that we need to measure both the moment, and the rotational velocity.

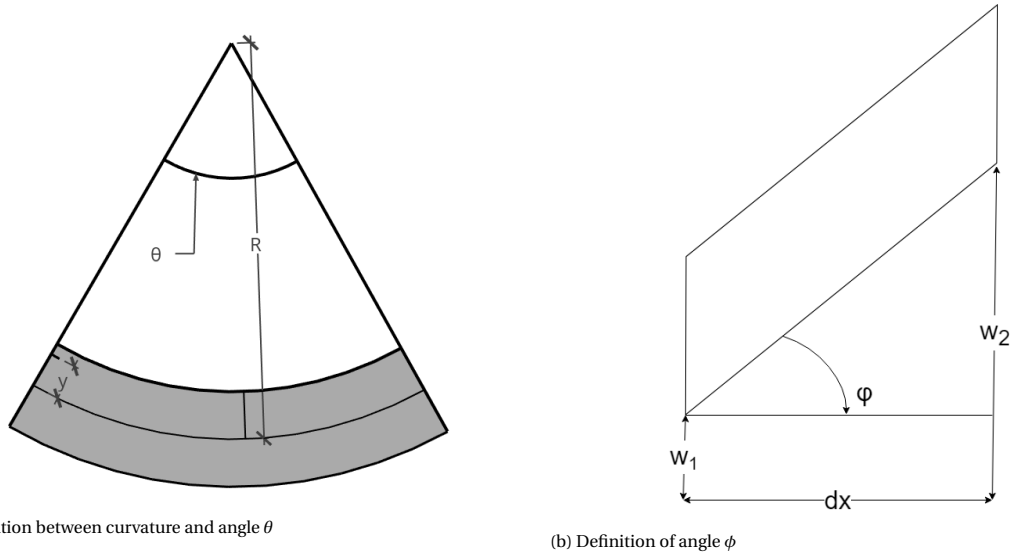
MOMENT - M (a) Relation between curvature and angle θ (b) Definition of angle ϕ

Figure 2.3: Geometrical relations

As described in section 2.3, the behaviour of the beam can be described by $M = EI \cdot w''$, where w'' is known as the curvature of the beam. According to EEBT this is related to the strains, with equation 2.15. Also see figure 2.3a. y is the distance to the centre line of the beam, in this case half the thickness. θ is the angle and finally ϵ is the strain.

$$\frac{d^2 w}{dx^2} = \frac{1}{R} = \kappa = \frac{d\theta}{dx} = \frac{\epsilon}{y} \quad (2.15)$$

In Euler-Bernoulli beam theory, the strains at the top of the beam are the same as the strains at the bottom. The y coordinate of these strain values is also known, this gives us the value of curvature κ , which is equal to the w'' . So, if the strains in the outer fibers are known, the moment at that location can be calculated.

ROTATIONAL VELOCITY - \dot{w}'

The rotational velocity is not directly calculable from the strains in the outer fibers. The angle $\phi = \frac{dw}{dx}$ does not depend on the strains in the outer fibers. However, ϕ can be derived from the difference in position between two points (see figure 2.3b). This means that the rotational velocity can be derived when w_1 and w_2 are known over time. These values can be obtained, as they can be derived from the accelerations, that are known over time. If we then divide the difference of the displacements into the distance between them, we know the angle ϕ . The time derivative of the now known ϕ will give us \dot{w}'

$$\frac{w_1 - w_2}{dx} = \phi = w' \quad (2.16)$$

It should be noted that the positions of w_1 and w_2 are to be close together. This means that dx will be as small as possible.

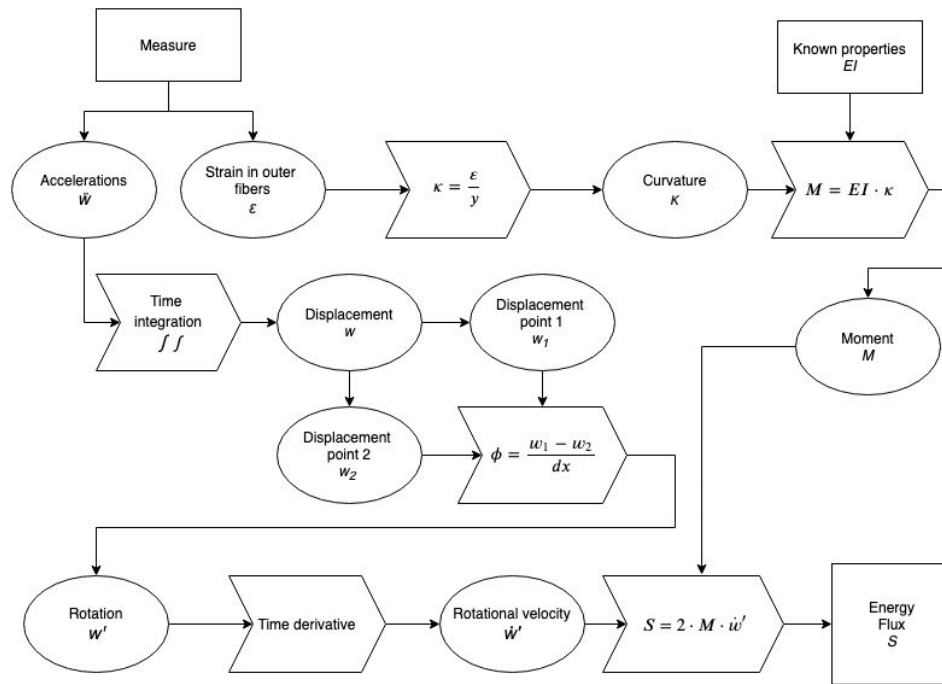


Figure 2.4: Flowchart of calculations

As shown in this chapter, the Energy Flux S at a certain point can be calculated with known strains at that point, and known accelerations close to each other. All steps from measurements to Energy Flux can also be shown in flowchart form, see figure 2.4. In this figure, the round blocks are variables that are known through measurements or calculations. The arrow blocks are equations used to derive said variables. The squares indicate the start or finished variable.

After the data has been processed. The result will be values of Energy Flux for every weight step at 3 places, plotted over time. The values of the Energy Flux can then be compared to each other.

3

NUMERICAL ANALYSIS

In the background chapter, a method of energy flux measurement is discussed. Now that that's known, the exact set-up of a numerical and physical experiment can be chosen. In this experiment a multitude of parameters should be set. Some of them should be the same in every iteration, and some of them should change between iterations. These parameters are discussed below.

3.1. SET-UP

The experiment can be seen as a proof of concept. The main questions it should answer are discussed in section 1. To ease the analysis the experiment should have as few unknowns as possible. Therefore, a few key properties of the application in a slip-joint are not taken into account to break the situation down to its easiest and most basic form. As discussed in section 2.3, this thesis will use EBBT. This theory simplifies the situation significantly. The curvature of the shell is ignored and simplified to a 1-dimensional situation. The beam will be simply supported, this support leads to the least amount of unknown forces at the boundaries of the beam. In conclusion, the setup discussed above is shown in figure 3.1.

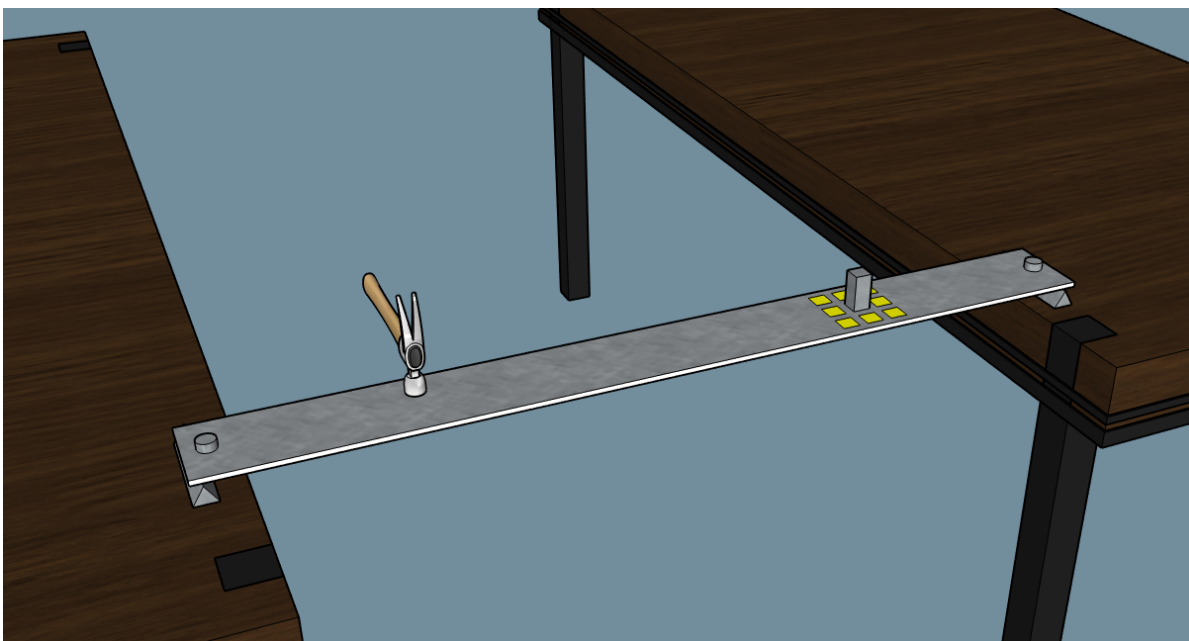


Figure 3.1: Example setup for the analyses.

3.2. BEAM PROPERTIES

Both the numerical analysis and the experiment investigate a vibrating beam. Some of the properties of this beam are given below. These properties are the same for both the experiment and the numerical analysis.

Beam property	Value
Length [m]	1
Width [m]	0.1
Height [m]	0.006
Cross-sectional Area [m^2]	0.0006
Density [kg/m^3]	7850
Young's Modulus [GPa]	200
Shear Modulus [GPa]	79.3
Bending stiffness EI [$N \cdot M^2$]	360
Shear stiffness GA [$N \cdot M^2$]	47580000

Table 3.1: Properties of the beam

3.3. NUMERICAL SIMULATION IN ANSYS

ANSYS is a multi physics engineering simulation software tool. The software is employed to calculate fluid dynamics and structural problems, that are based on discretization of the analyzed problems. For this thesis, ANSYS Workbench 19.1 was used.

Multiple analyses are possible within ANSYS. For this research, a transient structural analysis was done. This model consists of multiple building blocks, discussed in section 3.4. ANSYS can build up its model with various elements. For this study, Euler Bernoulli beam theory needs to be uphold. Therefore, BEAM188 elements were used. These elements have 6 degrees of freedom at each node, namely translation along three axes and rotation about three axes. This means that it is a Timoshenko beam element. However, in our model the shear modulus is so much larger than the bending stiffness, that the results will differ less than 0.003% (Department of applied Mechanics, Budapest University of Technology, 2018).

3.4. ANSYS MODEL

The ANSYS model consists of several parts. The properties of the model itself, meaning, among other things, the input of the model. These are the properties with which the modal analysis of the system was done. Secondly, the load properties are discussed. These are only used in the transient structural analysis. Lastly, the type of output of the model is quickly described.

3.4.1. MODEL DESCRIPTION

In this section, the developed model is described. The focus is on determining input parameters, such as sampling frequency and mesh size, beam parameters, measurement locations, contact points and damping.

Determining sampling frequency and mesh size

For the determination of the necessary sampling frequency, the eigenfrequencies of the beam are needed. A modal analysis calculates these eigenfrequencies. The results for the first six eigenmodes can be found in table 3.2.

Mode	Frequency [Hz]
1	21.93
2	55.008
3	136.32
4	184.52
5	220.7
6	359.65

Table 3.2: Eigenfrequencies of the beam

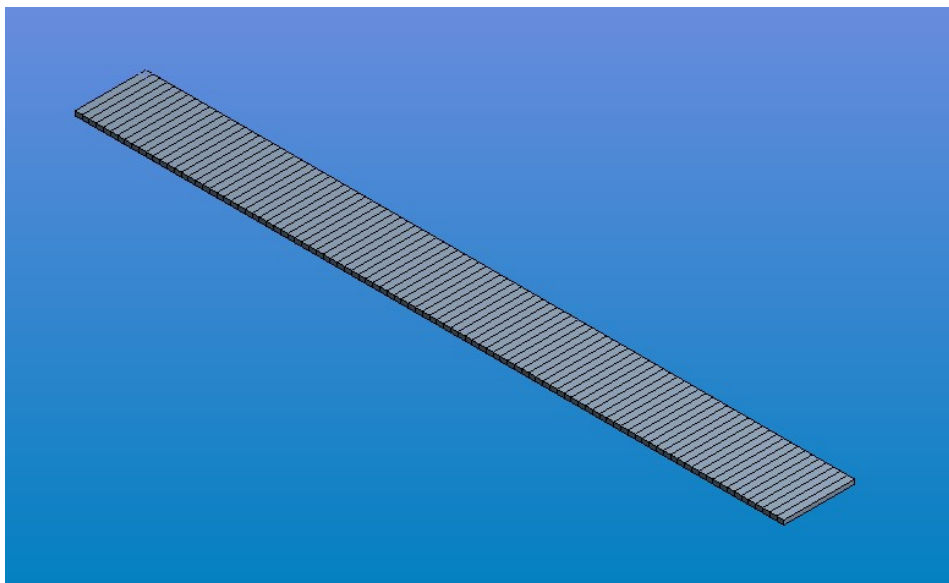


Figure 3.2: ANSYS model for the numerical analysis, with the 3-dimensional representation shown. The actual mesh is 1-dimensional. Supports are present, but not shown in this figure.

To correctly assess the movement of the beam, at least eight samples are needed during the eigenperiode of the highest relevant eigenfrequency. As a first estimate, eigenmodes higher than the sixth are not expected to play any significant role in the behaviour of the beam. The sampling speed for the first model will then be

$$T = \frac{1}{359.65} = 0.00278 \text{ s} \quad (3.1)$$

$$\Delta t = \frac{0.00278}{8} = 3.475 \cdot 10^{-4} \text{ s} \quad (3.2)$$

Using this time step the first analysis was done. The beam was excited with a temporal force. From the Fourier Analysis, it could clearly be seen that the vibration almost completely consists of the first two eigenfrequencies, making such a small time step unnecessary. Consequently, a larger time step of $\Delta t = 1 \cdot 10^{-4}$ was chosen afterwards.

The determination of the mesh size was an iterative process. The mesh size was increased step-wise, until no more changes in behaviour were seen. At this point, the mesh size was assumed to be sufficient. This ended in a mesh size of 0.01 meter. The meshing was performed using a sweep mesh method. This method ensures that the model consists of elements of equal size. This resulted in the symmetrical mesh presented in figure 3.2. The mesh is symmetrical about all axis from the midpoint of the beam.

Beam parameters

The beam has a length of 1000 mm, a width of 100 mm and a thickness of 6 mm, as was presented in table 3.1. At both ends the beam is simply supported. Meaning that one of the edges of the mesh is fully supported, restricting movement in all directions, but allowing for rotation. The beam is made of structural steel class S460, with a density of $7850 \text{ kg} \cdot \text{m}^{-3}$.

Measurement locations

To get an overview of the behaviour of the Energy Flux along the beam, eleven locations for the calculation of Energy Flux were determined. These locations were placed in such a way, that they are evenly spread, and there is a measurement location close to both supports, and midpoint. All eleven locations are shown in figure 3.3.

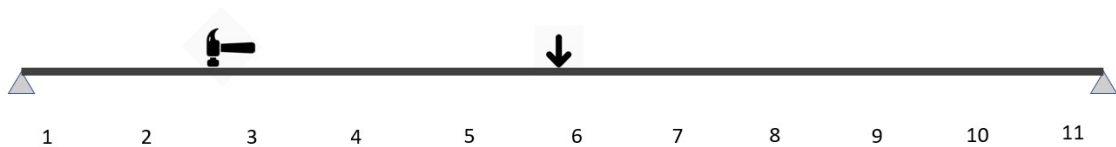


Figure 3.3: Mechanical Model with the measurement locations

Contact point

The contact point is modelled by adding a point weight at a certain location along the beam. The amount of weight was increased step wise. In an one-dimensional model the size of the contact area cannot be changed because, evidently, a point weight cannot increase in size. Therefore, influences of contact area size will not be discussed.

To determine the influence of the location of a contact point, four different Point Load Locations (PLLs), were determined. These PLLs are shown in figure 3.4. PLL 1 is at the midpoint of the beam. PLL 2, 3 and 4 are on measurement locations 7, 8 and 9, respectively.

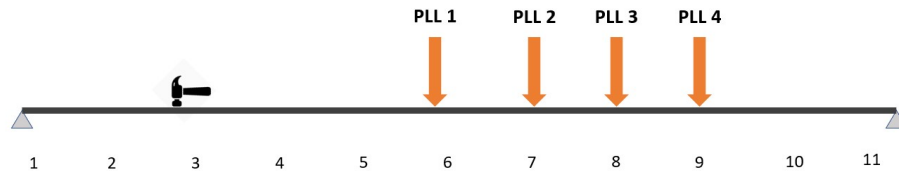


Figure 3.4: The location of point load locations 1, 2, 3 and 4. PLL 1 is located at the midpoint of the beam.

Damping

Any form of pulse load, will introduce a spectrum of frequencies into the system. Some of these frequencies will be very high. Due to the short wavelength of these high frequencies, they will dissipate more quickly than the lower frequencies. In the model, this effect is imitated using numerical damping. This kind of damping makes sure that the higher frequencies of the model decay. Because numerical damping is fictional damping, the damping coefficient should not be very large to achieve the correct response of the system. The value of 0.0005 was chosen, the exact magnitude of the coefficient showed little influence in this order of magnitude.

LOAD DESCRIPTION

The model runs for 4 time-steps. The first three time-steps are 0.01 seconds, the last time-step is 4.97 seconds. The hammer blow is modelled by applying a force during one of the time steps. The force increases linearly to 100N during time step 2, and linearly decreases back to 0N in time step 3. During all other time steps this force is absent.

OUTPUT DESCRIPTION

Once the input of the ANSYS model is provided, the parameters to output are set. ANSYS can calculate deformations, forces and velocities directly. So there is no reason to use the method described in section 2.4.1. The Energy Flux is directly provided by the model. The Energy Flux is given as a direct output using the moment, the rotational velocity, the shear force and the directional velocity.

However, to compare the numerical results to the experimental results, another extraction of Energy Flux is done. This method replicates the experimental method. The strains are calculated at both ends, with which the moment is calculated. The rotational velocity is calculated using the deformation at two places. These results are discussed in section 5.2.2. The data processing and visualization have been done using MATLAB.

4

EXPERIMENTAL APPROACH

The overall set-up has already been discussed in section 3.1. The experimental approach is very similar to the numerical approach. The requisites and the way to build up to a final design are discussed in this chapter.

4.1. EXPERIMENT REQUISITES

Most of the experiment requisites need no further introduction, and are simply summed up here. Five of them are discussed in further detail below, namely the weights, the hammer, strain gauges, accelerometers and ADC.

- Analog-to-digital converter (ADC)
- Weights
- Laptop with Mp3 software
- Cables
- Support Structure for the beam
- Simply supported connection
- Beam
- Strain gauges
- Accelerometers
- Media to attach weight

Weights

The weights will be used to model a contact area. This weight will distribute its weight over its area on the beam. This way, both the area size, and the area pressure can be changed between experiments. To ensure that the weight will remain attached to the beam, the **Vaseline** will be used to join them together.

Hammer

The hammer to be used in the experiment has its own accelerometer and force measurement device built in. Using this data, the energy input of the hammer can be calculated.

Strain gauges

A strain gauge is a sensor that is used to measure strain on an object. The resistance of the device varies with applied force. The force is converted into electrical resistance, which is a property that can be measured. Strain gauges are glued on a specific spot on the beam and can therefore only be used once. Strain gauges can be attached in multiple ways. Because only bending stresses are relevant for this research, the strain gauges will measure the strain along the beam, and not perpendicular to the length of the beam. Furthermore, the

strain gauges can form a so called 'bridge'. These bridges come in three variations, which all only use one channel. Each bridge has its own applications. Depending on these applications, multiple configurations are possible. These are shown in figure 4.1

- **Full Bridge** - Two strain gauges at both sides of the beam.
- **Half Bridge** - One strain gauge at both sides of the beam.
- **Quarter Bridge** - One strain gauge at one side of the beam.

A fundamental parameter of the strain gauge is its sensitivity to strain. This is expressed as the gage factor (GF), which is the ratio of relative change in the electrical resistance R to the mechanical strain ϵ .

Ideally, the resistance of the strain gauge only changes due to the applied strain. However, the resistance of the strain gauge is not perfectly constant. This can be caused by changes in temperature, or other small variations in its environment. This signal is called noise, and the expected signal should be at least five times as large as the expected noise. The expected strains can be calculated by the numerical model.

The strain gauges that will be used are, naturally, not perfect. A certain amount of random 'output' is expected. When the strains are too little, the only output will be this so called noise. For the output to be interpretable, a minimum amount of strain is needed. This is called the Signal-to-Noise ratio (S/N ratio). When this ratio is too low, the output will mean nothing. For the Energy Flux to be measurable, this S/N ratio should exceed a value of 5. The actual expected signal largely depends on the hammer blow. With an impact of 100N, for 0,01 seconds, the expected strains at the top and the bottom of the beam are approximately $2 \cdot 10^{-4} [m/m]$. The noise of a standard full bridge strain gauge is around $20 \mu m$. This gives a S/N ratio of 10, at most points in time. As long as the S/N ratio is larger than 5, the signal is good. This means that, numerically, the signals are large enough for Energy Flux measurements.

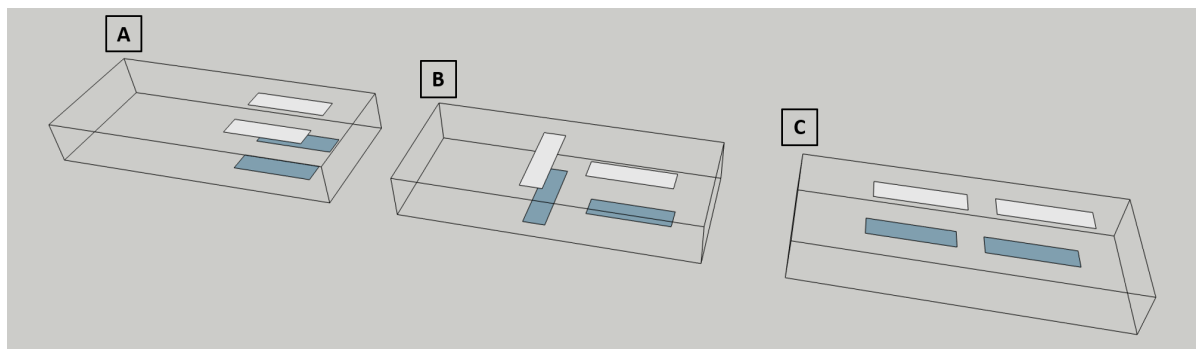


Figure 4.1: Configuration options for a full bridge strain gauge

Accelerometers

An accelerometer is a sensor used to measure acceleration forces. These forces can be static, like continuous or gravity forces, or dynamic, like vibrations. They measure in meters per seconds squared (m/s^2) or in G-forces (g). Accelerometers are made of many different components and communicate over an analog, digital or pulse-width modulation interface.

When choosing an accelerometer, the range of the device is important. Ranges vary between more or less 1g to 250g. Smaller ranges are more sensitive. The accelerations expected in the experiment can be check in the numerical model. After this, an appropriate accelerometer can be chosen.

Analog-to-Digital Converter

Analog-to-Digital converters (ADC) are devices that convert analog signals into digital signals. These machines take the output of the strain gauges and the accelerometers as an input, and output digital signal, a computer can interpret. However, these devices have a maximum amount and frequency of input. The ADC's available at the TU Delft can process nine channels simultaneously. Accelerometers and strain bridges (full or half), all consist of one channel. This puts a maximum on the amount of data that can be acquired in one experiment.

4.2. BUILDING BLOCKS OF THE EXPERIMENT

The second research question introduced in section 1.3, was "How can the numerical results be validated in an experiment?". This research question requires several sub-questions. Each of these questions will provide a building block for the experiment. Using these building blocks the final experiment can be composed. The questions and their necessary building blocks are discussed below.

Is Energy Flux measurable?

This question is already partly answered in section 2.4.1. However, in that section, a new equation for Energy Flux is given, namely $S = 2 \cdot M \cdot \dot{w}'$. This is because the shear force is difficult to measure at a specific point. Since we know that $\frac{dM}{dx} = V$, the original equation for the Energy Flux might also be measurable, **with two strain gauges close to each other, V can be approximated**. These measurements can afterwards be compared to the numerical model.

The equations for the numerical analysis, and the experimental analysis are slightly different. For a proper comparison, there are two necessities. A numerical analysis using the equation for the experiment, and the measurement of the shear force in the experiment. A numerical analysis with the experimental equation has been done. Most of these results can be found in Appendix. Once the experiments have been done, the results can be compared to the numerical results. In the experiment, the shear force should also be computed. This can be done by measuring the moment at two locations close to each other. **Therefore, the experiment should have strain gauges, close to each other along the length of the beam, a full bridge strain gauge in configuration C.**

Is Euler-Bernoulli Beam Theory applicable?

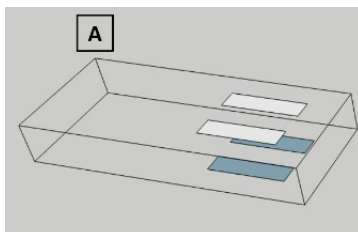
As discussed in section 2.3, EBBT makes a few key assumptions that need to be validated. First of all, EBBT assumes a linear elastic stress line, along the cross-section of the beam. This will result in equal and opposite strains at both sides of the beam. To check this, **full bridge strain gauges are needed**. Secondly, EBBT assumes no changes in behaviour along the width of the beam. To check this assumption, **multiple Energy Flux equations have to be done, along the width of the beam**.

Are the numerical results representative for the experimental results?

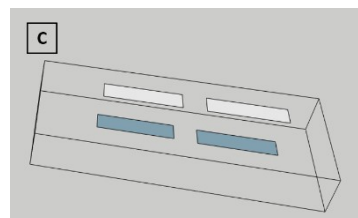
To get a good understanding of how realistic the numerical analysis is, a proper comparison has to be made between the numerical results, and the experimental results. Therefore, the experimental setup should be comparable to the numerical model. Depending on the results of the numerical model, a few locations on which Energy Flux should be measured in the experiment should be chosen.

In conclusion, the experiment should consist of these things

- A full bridge strain gauge in configuration A at a measurement location.
- A half bridge strain gauges, at all measurement locations.
- A full bridge strain gauge in configuration C at a measurement location.
- Two accelerometers, at all measurement locations.
- A point at which a weight can be attached.



(a) Configuration A



(b) Configuration C

Figure 4.2: Strain configurations to be used in the experiment

5

RESULTS

The results of the methodology discussed above are twofold. In the first part, the results of the numerical analyses are discussed. Secondly, a clear plan is described for the numerical results to be experimentally validated.

5.1. NUMERICAL RESULTS

From the numerical model, lots of data were acquired. These data described the behaviour of Energy Flux, which can be analyzed in different manners. First of all, the behaviour of EF over time can be studied. This signal consists of several frequencies, which can be studied in the frequency-domain. Finally, the importance of frequencies over time may provide additional information on the presence of contact areas. This can be studied in the time-frequency-domain. Subsequently, results are divided into three sections: (1) time-domain, (2) frequency-domain and (3) time-frequency-domain. All these sections are divided into two parts. Firstly, 'the general behaviour' is studied, where no point load is added to the system. Secondly, the influence of the location and the magnitude of the weights are discussed. To understand the influence of a simulated contact area, the first section describes the global differences of a system with and without a point load.

5.1.1. INFLUENCE OF POINT LOAD ON SYSTEM PROPERTIES

Before analyzing the numerical results, it is important to understand the changes in the system properties caused by a point load anywhere in the system. The two main system properties discussed here are the energy input and the eigenfrequencies.

Energy Input

The energy input of the system is given by the force of the hammer, multiplied by the velocity at the point of impact. The added point load influences the velocity of the beam at the point of impact, and therefore also the energy put into the system. For this study, the point load can have multiple locations and magnitudes. The parameters of the hammer blow are kept constant, meaning the location and the force of the hammer are the same for every simulation.

	0kg	1kg	2kg	3kg	4kg	5kg
PLL 1	160.8	151.7	146.0	142.0	139.2	137.0
PLL 2	160.8	162.1	163.1	163.4	163.8	164.2
PLL 3	160.8	171.3	178.2	182.9	186.2	188.6
PLL 4	160.8	173.4	184.9	193.9	200.9	206.5

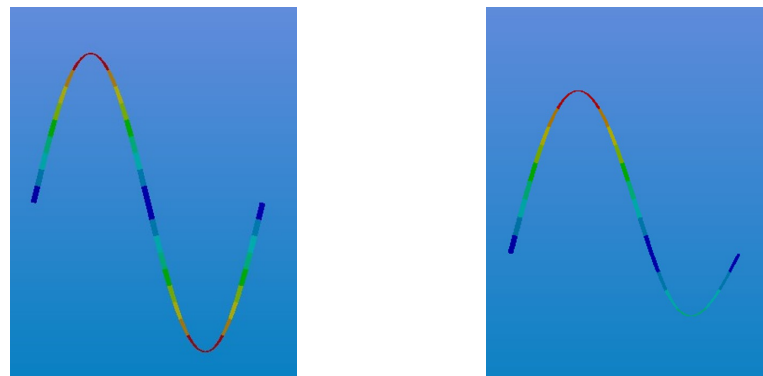
Table 5.1: Overview of Energy Input for every system, expressed in Joule. PLL refers to the location of the point load. For all locations six magnitudes were studied, ranging from 0 to 5 kilograms.

Table 5.1 shows the energy input for four different locations of point loads. The energy input depends on the locations and the magnitude of the point load. The four different PLL's can be found in figure 3.4.

Naturally, when the magnitude of the point load is 0 kg, the location is irrelevant, because the system does not change. Table 5.1 shows that the energy input equals 160.8J, when no point load is added. In case of PLL 1, located at the middle of the beam, the increase of magnitude of the point load results in a decrease of energy input. In case of PLL 2, the changes in energy input are small, but an increase can be seen. For PLL 3 and 4 the increase of added weight results in a clear increase of energy input. When comparing PLL 3 and 4, a larger distance from midpoint results in a larger increase of energy input.

Eigenfrequencies

The eigenfrequencies depend on the eigenmode shapes. These are strongly influenced by the presence of a point load. This effect can be seen in figure 5.1. 5.1a shows the second eigenmode shape of the system without any point loads can be seen. In figure 5.1b the second eigenmode shape of the system with a 4 kilogram point load at PLL 3 is shown.



(a) Second eigenmode of the system without a point load. (b) Second eigenmode of the system with 4kg at PLL 3.

Figure 5.1: Effect of the point load on the shape of the second eigenmode.

Table 5.2 shows the eigenfrequencies of all the simulated systems. An increase in weight results in a decrease in eigenfrequencies. However, there is one exception. In case of PLL 1, the second eigenmode shape is not influenced by the point load. As can be seen in figure 5.1, the midpoint of the beam does not move in the second eigenmode. Because of this, a point load at this location does not influence the second eigenfrequency.

PLL 1	0kg	1kg	2kg	3kg	4kg	5kg
1st eigenfrequency	13,732	11,497	10,082	9,0854	8,335	7,744
2nd eigenfrequency	54,918	54,918	54,918	54,918	54,918	54,918
3rd eigenfrequency	123,53	107,89	101,35	97,792	95,553	94,016
PLL 2	0kg	1kg	2kg	3kg	4kg	5kg
1st eigenfrequency	13,732	11,726	10,387	9,4166	8,6736	8,0816
2nd eigenfrequency	54,918	51,264	49,455	48,386	47,683	47,185
3rd eigenfrequency	123,53	120,26	118,61	117,63	116,98	116,53
PLL 3	0kg	1kg	2kg	3kg	4kg	5kg
1st eigenfrequency	13,732	12,243	11,123	10,25	9,5489	8,9711
2nd eigenfrequency	54,918	47,624	44,178	42,193	40,907	40,009
3rd eigenfrequency	123,53	120,02	118,63	117,88	117,43	117,11
PLL 4	0kg	1kg	2kg	3kg	4kg	5kg
1st eigenfrequency	13,732	12,945	12,254	11,645	11,109	10,633
2nd eigenfrequency	54,918	47,562	43,187	40,376	38,438	37,03
3rd eigenfrequency	123,53	109,09	103,89	101,32	99,801	98,802

Table 5.2: Eigenfrequencies of the various systems

5.1.2. TIME-DOMAIN

An example of Energy Flux in the time-domain is given below. In this figure, a few things should be noted. First of all, the Energy Flux slowly decreases. This is due to damping. Secondly, there are multiple frequencies important in this signal. An analysis of these frequencies is done in section 5.1.3. Lastly, it could be that the importance of certain frequencies decreases over time. An analysis of these effects is done in section 5.1.4

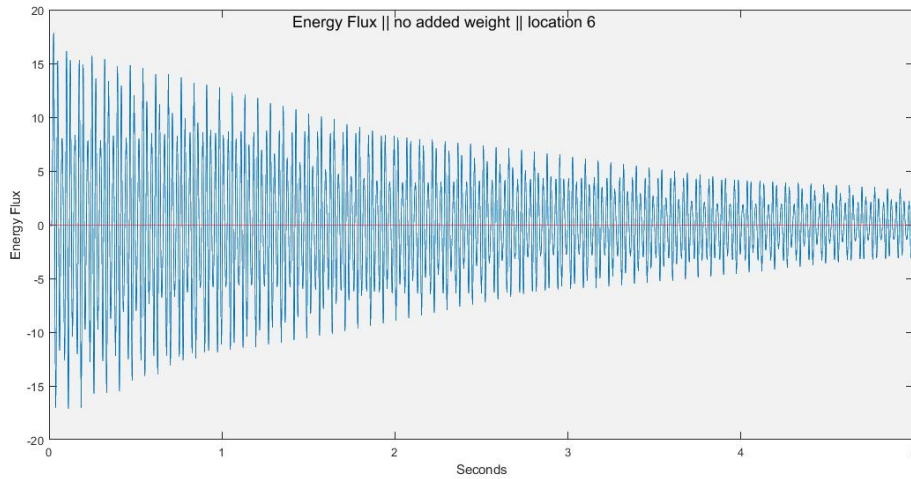


Figure 5.2: Example of Energy Flux in the time-domain

Figure 5.2 shows an example of what Energy Flux looks like through the cross-section at midpoint in the time-domain. Energy Flux behaviour depends heavily on the examined cross-section. In figure 5.3 the behaviour at all locations can be examined. To ease the comparison, the y-axis is kept the same across all subplots. It can be clearly seen that the more energy flows through the middle sections of the beam.

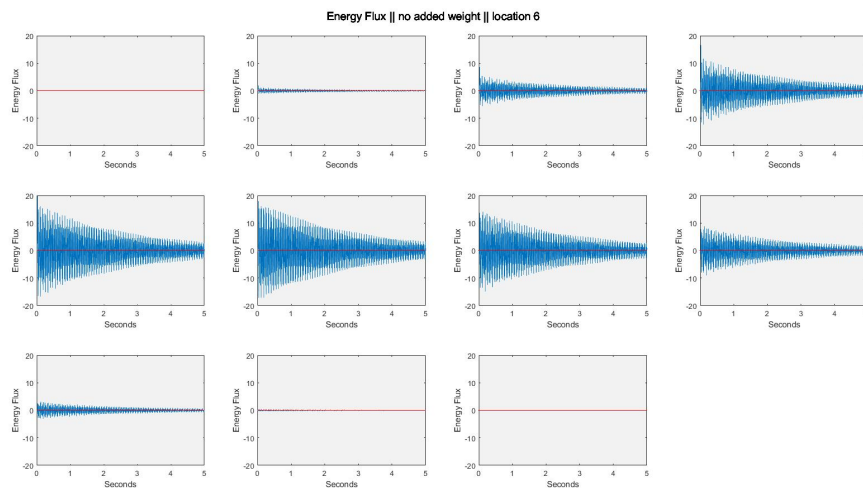


Figure 5.3: Example of Energy Flux through all locations

As discussed earlier, Energy Flux is a vector. When plotted over time, the direction is given by the sign of the scalar (above or below 0). All values above zero indicate an Energy Flux in a positive direction, in this case to the right. Values below zero indicate flux in the opposite direction, in this case leftward. When this signal is then integrated. The complete energy through this cross-section can be calculated. A cumulative integration would mean to subtract negative Energy Flux from the positive Flux. Again, this Cumulative Energy Flux (CEF) can be plotted. The behaviour of these plots is described using three examples.

- **CEF through location 3, see sub-figure A.1a.**

At the start, a large amount of energy is transported rightwards. After this, the EF simply fluctuates. The amplitude of this fluctuation is not very large. The signal is mostly composed of three frequencies: the first, the second and the second minus the first

- **CEF through location 6, see sub-figure A.1b.**

This behaviour resembles the behaviour through location 3, with the exception that the amplitude has increased. Towards the middle, the amplitude of these plots always showed an increase. The signal importance of the first eigenfrequency has decreased. Meaning that this signal is mostly composed of two frequencies: The second, and the second minus the first.

- **CEF through location 9, see sub-figure A.1c.**

Except for the absence of the large amount of energy transported rightwards in the beginning, this behaviour strongly resembles figure A.1a. Both signals are made up of the same frequencies, and have similar amplitudes.

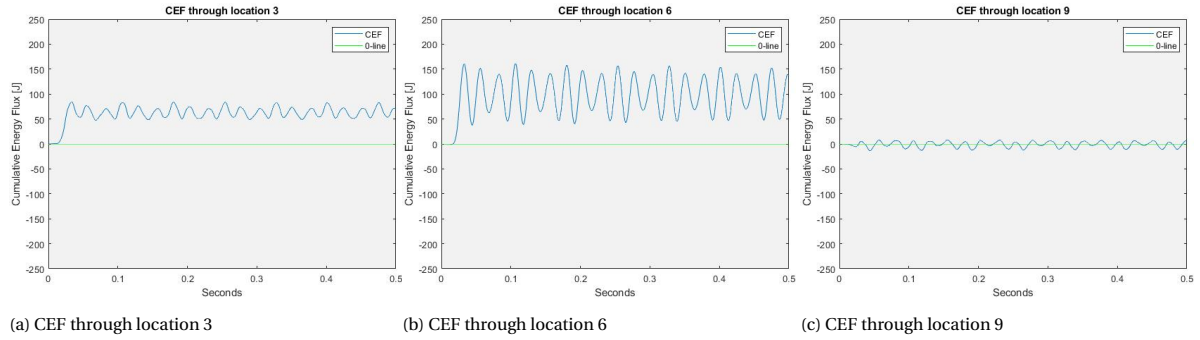


Figure 5.4: Cumulative Energy Flux through three locations, without added weight.

Location of a contact point

With the added weight, the amplitudes of Energy Flux increases. Not only on the location of the weight, but also on the neighbouring locations. When the signal is normalized with respect to the absolute mean value of the original signal, these differences become clear, see table 5.3. In this table, the Mean Absolute Values (MAV's) of EF of the system with, and without weight are compared. This is done for all PPL's. Around a point load locations, a more clear increase in MAV is seen. However, the highest increase is not always at the location of the point load. Lastly, it should be noted that the increases are less significant for PPL 1, than for the others.

	$ \overline{0kg} / \overline{2kg} $ PPL 1	$ \overline{0kg} / \overline{2kg} $ PPL 2	$ \overline{0kg} / \overline{2kg} $ PPL 3	$ \overline{0kg} / \overline{2kg} $ PPL 4
Location 1	1.0279	1.3238	1.1956	1.0367
Location 2	1.0260	1.3305	1.2076	1.0495
Location 3	1.0471	1.3740	1.2597	1.0941
Location 4	1.0790	1.4416	1.3474	1.1689
Location 5	1.1248	1.5326	1.4802	1.2853
Location 6	1.1678	1.6500	1.6822	1.4712
Location 7	1.1060	1.6266	2.0221	1.7976
Location 8	1.0685	1.2519	2.3006	2.5654
Location 9	1.0410	1.1679	1.5213	4.2340
Location 10	1.0249	1.1287	1.4269	2.0969
Location 11	1.0317	1.1367	1.4371	2.1107

Table 5.3: The increase of mean absolute value of the Energy Flux, at all locations for all point load locations

This increase in amplitude is also illustrated in figure 5.5. In this figure, the normalized Energy Flux is plotted. At every moment in time, the value of EF is divided by the MAV of the EF at that location without any added

weight. To ease the comparison, two red lines are plotted at values of 5 and -5 . At the exact location of the weight, the EF plot looks differently, the EF becomes mostly positive, which would indicate a large flow of energy towards the support. Besides this, no clear difference can be identified. An increase at neighbouring locations for example, cannot be seen. So besides a change at the exact PLL, when looking at the time-domain alone, the location of a contact point cannot be identified.

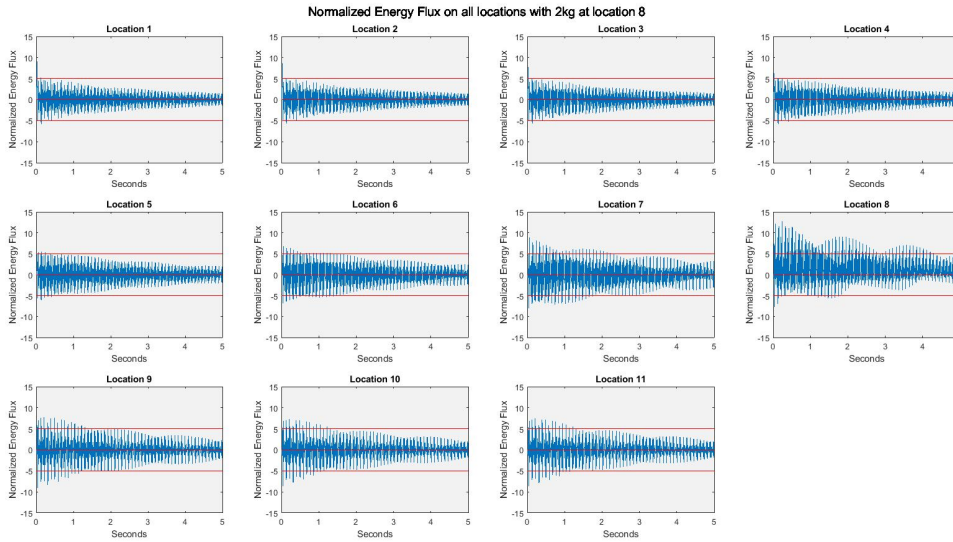


Figure 5.5: Normalized Energy Flux on all locations, with 2kg at location 8

When looking at the CEF, the differences are similar. At the exact location of the point load, the CEF looks completely different. At all other locations, the differences are smaller. For two situations these differences are illustrated in figure 5.6. The figure shows the CEF through three cross-sections, without any added weight, and with two kilogram at PLL 3. In the sub-figure 5.6a, a small increase in amplitude, and a change in frequencies can be seen. The increase in amplitude is much larger at location 6, in sub figure 5.6b. The CEF at the location of the point load, is completely different. This effect could also be seen in figure 5.5. In that figure the EF becomes mostly positive, resulting in a large amount of EF moving rightwards. This can now be seen also be seen in figure 5.6c.

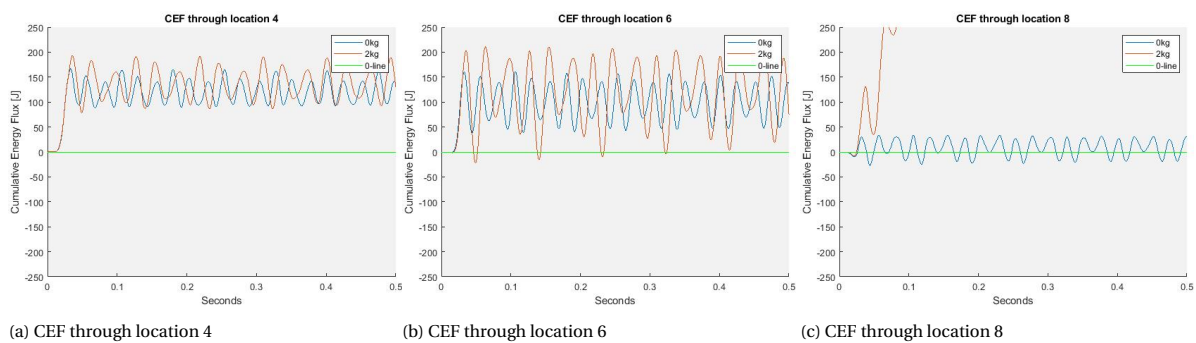


Figure 5.6: Cumulative Energy Flux through three locations, without added weight.

Magnitude of the weight

As described before, the presence of a point load increased the amplitude of the CEF. The magnitude of this point load, simply increased this effect. However, the increase also depended on the location along the beam, as can be seen in figures 5.8 and 5.7. The increase seems to depend on the proximity to the middle, and to the weight. Meaning that both closer to the weight, and closer to the middle, the magnitude of the point load had more influence.

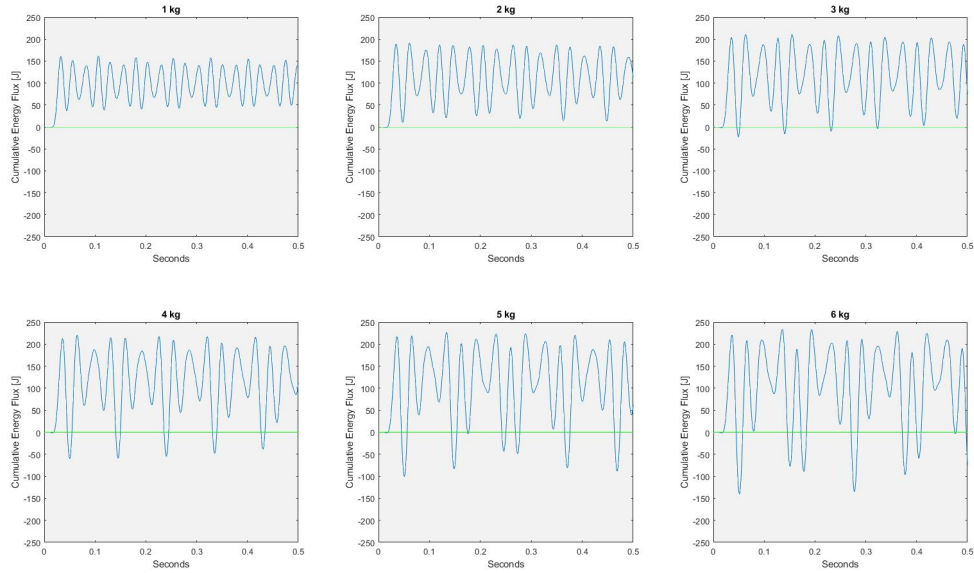


Figure 5.7: Cumulative Energy Flux through location 6, with increasing weight at location 8

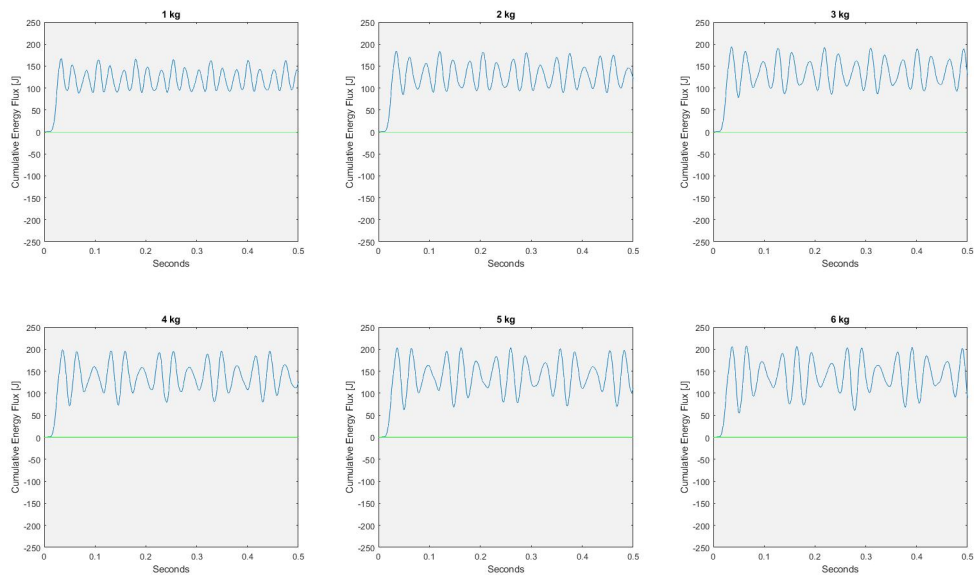


Figure 5.8: Cumulative Energy Flux through location 4 with increasing weight at location 8

5.1.3. FREQUENCY-DOMAIN

The Energy Flux in the time-domain clearly consists of multiple frequencies. To examine which frequencies are important, a Fourier analysis is done. A fast Fourier transform decomposes a function into its constituent frequencies. The results display which frequencies are important in the five-second signal. First, the behaviour of the frequencies will be discussed without any additional weight. When this behaviour is clear, the influence of a simulated contact point is discussed. First the location of the weight, and then the magnitude of it.

When multiplying two sinusoids that consist of two pure frequencies, the outcome consists of four frequencies. When the sinusoids are not longer pure, the outcome is expected to consist of six frequencies. The first, twice the first, the second, the second minus and plus the first, and twice the second. These are the six peaks, expected to be visible in a Fourier analysis. Naturally, not all frequencies will be visible at every location, because the importance of each component of the Energy Flux will vary depending on location.

However, when no weight is added to the system, the six peaks are not all located at those frequencies. The frequencies can be seen in figure 5.9. The peaks are discussed below.

- Peak 1 - 13.8 Hz - This peak is at the first eigenfrequency, as expected.
- Peak 2 - 40.6 Hz - This peak is at the second eigenfrequency, minus the first frequency, a peak here was expected.
- Peak 3 - 54.4 Hz - This peak is at the second eigenfrequency, as expected.
- Peak 4 - 63.4 Hz - This peak is not at the second eigenfrequency plus the first eigenfrequency. It is five Hertz too low.
- Peak 5 - 104.2 Hz - This peak is not at twice the second eigenfrequency, but again five Hertz too low.
- Peak 6 - 117.8 Hz - This peak is also not at any of the predicted locations. It should be noted that it is exactly the first eigenfrequency higher than peak 5.

Besides the odd placement of peaks four, five and six, the absence of two expected peaks is also worth noting. No peaks are visible at twice the first, and twice the second eigenfrequency. At twice the second eigenfrequency, absolutely nothing was visible, even without the presence of a high peak nearby. However, at twice the second eigenfrequency, a small peak was found at some locations, especially when the third peak was lower. Because of the height of the third peak, specifically in the middle, it is possible that the peak at twice the second eigenfrequency was too low to be noticeable, even though it was actually there. This is illustrated in figure 5.10.

Without any point loads, these peaks always appear at the same places. This is also illustrated in figure 5.9. This figure shows all peaks, at all locations. The heights of the peaks vary, but the locations of the peaks are constant over the entire length.

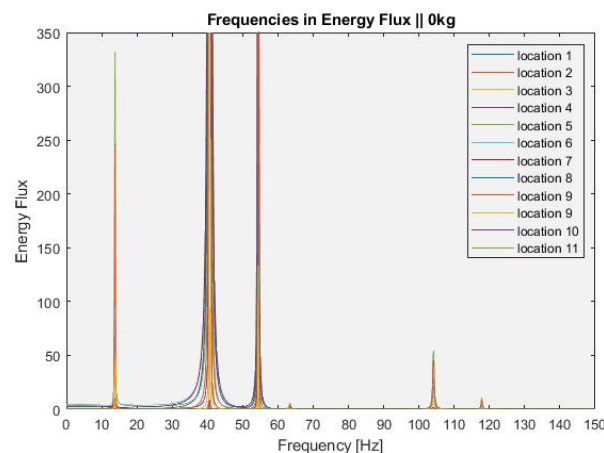


Figure 5.9: Example of a Fourier analysis of Energy Flux through location 7. In this example, no weight was added

It should also be noted that above 110 Hz, no other peaks could be distinguished. This indicates that for this structure, only the first two eigenmodes play a role.

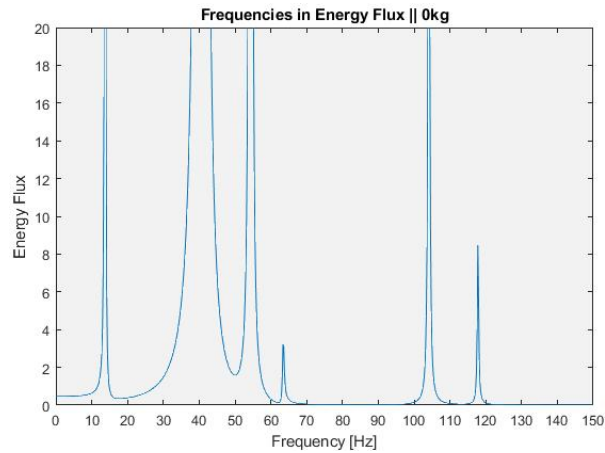


Figure 5.10: Example of a Fourier analysis of Energy Flux through location 7. In this example, no weight was added

The heights of these peaks vary, depending on the location of the analysis. This height can be plotted over the length of the beam. This is illustrated in figure 5.11. Over the length of the beam, 11 locations were chosen to calculate Energy Flux. The positions and numbering of these locations have already been discussed in section 3.4, and can be seen in figure 3.3. To get a complete picture of how the entire beam behaves all locations were examined. First, the behaviour is analyzed with no added weight. In this analysis, 6 peaks were analyzed.

The first four peaks are the peaks at the expected locations, for peak five and six, the closest peak was analyzed, because at the expected locations, no peak was found.

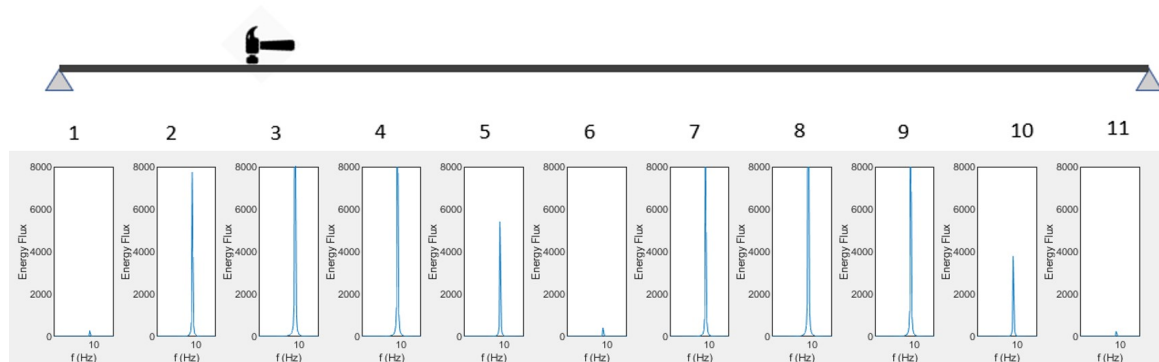


Figure 5.11: The height of the peaks along the length of the beam

The first peak, at the first frequency, is most important at 1/4 and 3/4 of the beam. This can be logically explained by the fact that, when getting closer to the middle, there is no rotational velocity in the first eigenmode, the Energy Flux at that point will therefore become zero. The second peak is too small to distinguish, and is therefore not taken into account here. For the fourth peak, at the second eigenfrequency, the amplitude increases towards the middle. Furthermore it should be noted that the third and the fifth peak are a combination of the first and the second eigenfrequency. The third peak is the highest by far, with the peak in the middle being five times as large as any other peak.

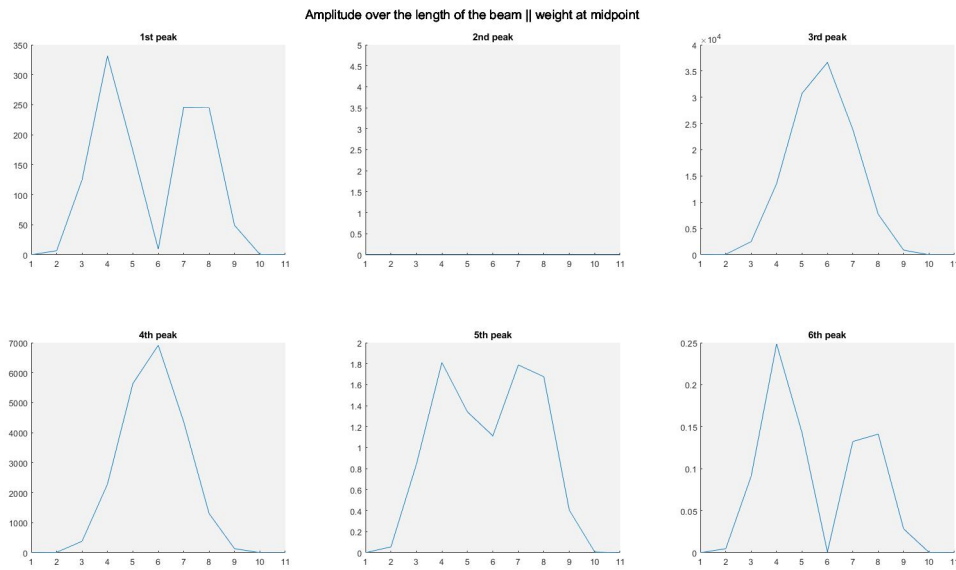


Figure 5.12: The behaviour of all peaks over the length of the beam

Presence of a weight

When a point load is present in the system, regardless of its locations and magnitude, a few things change in the Fourier analysis. This situation is illustrated in figure 5.13. First of all, there now is a clear peak at twice the first eigenfrequency. Secondly, the location of the previous peak 4, is now at the second plus the first eigenfrequency, where it was expected. The height of the peaks depends on the location of the weight. This is described below.

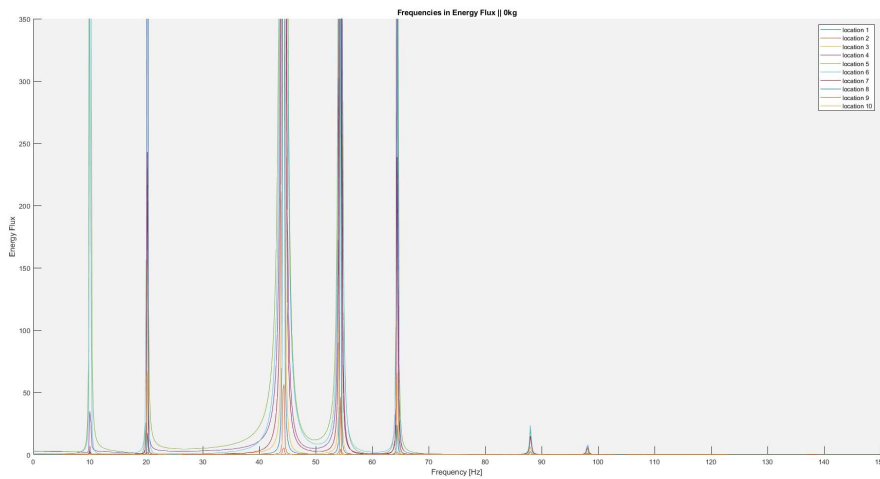


Figure 5.13: Example of a Fourier Analysis of Energy Flux through all locations. With 2kg on PLL 2

Location

First the influence of the location of the weight is examined. For a first estimate, one can simply compare Fourier analyses at the location of the weight, and at any other location. As discussed before, the outcome of a Fourier analysis consists of 6 peaks. With weight, the expected six peaks are seen.

However, when looking at the Fourier analysis at the exact location of the weight, it looks different. An example is given in figure 5.14. Now a peak can be seen at every multiplication of the first eigenfrequency. This is only when the Fourier analysis is exactly at the location of the weight, one node next to the location the Fourier analysis looks like all other locations. When looking at the behaviour over the length of the beam, these additional peaks are ignored, because they only occur at the location of the weight.

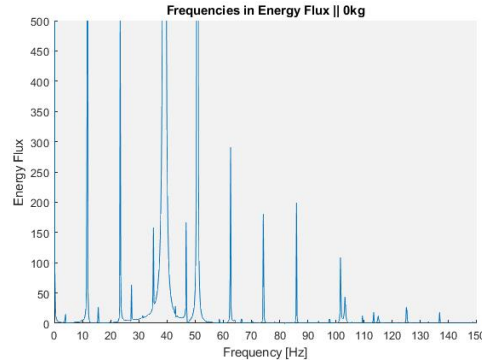


Figure 5.14: Zoomed in example of a Fourier analysis at the location of the weight

The location of the last peaks also depends on the location of the weight. For every PLL the two peaks around twice the second eigenfrequency, seen in figure 5.9, were, albeit small visible. However, their locations differed. For PLL 2, 3 and 4, a peak was also seen at twice the second eigenfrequency. This peak was significantly larger than the other two peaks, but still substantially smaller than the earlier peaks.

This means that, for PLL 2, 3 and 4, there are three peaks above 80 Hz. One at twice the second eigenfrequency, and two at slightly higher frequencies. The locations of the latter two peaks, for 1 kilogram on all PLLs are given in table 5.4. Because the behaviour of these peaks differs per PLL, they are all discussed separately.

- **PLL 1** - Above 80 Hz, there are two peaks. These peaks are separated by the first eigenfrequency.
- **PLL 2** - Above 80 Hz, there are three peaks. One at twice the second eigenfrequency, one at 102.6 and one at 103.2 plus the first eigenfrequency.
- **PLL 3** - Above 80 Hz, there are three peaks. One at twice the second eigenfrequency, one at 102.6 and one at 102.6 plus the first eigenfrequency.
- **PLL 4** - Above 70 Hz, there are three peaks. One at twice the second eigenfrequency, one slightly lower, and one slightly above that. The latter two are separated by the first eigenfrequency.

	Second to last peak	Last peak
PLL 1	92.6	104
PLL 2	103.2	115
PLL 3	102.4	114.8
PLL 4	94.4	105

Table 5.4: The location of the last two peaks, for 1 kilogram at each PLL

Figure 5.12 can also be made with a weight added to the system, see figure 5.15. In these figures, a comparison has been made between the behaviour with, and without a weight. Both are plotted, for a weight of 2kg at two locations. The y-axis is scaled the same for all locations to ease the comparison. For PLL 1, the sixth peak was ignored.

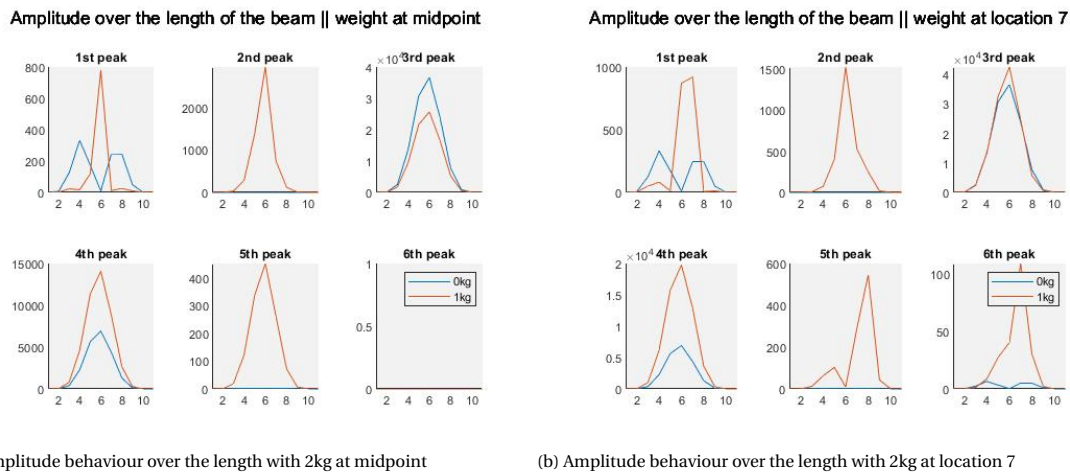


Figure 5.15: Comparison between the amplitudes of the FFT peaks, with and without added weight

The properties of the Energy Flux change, with the presence of a point load. The characteristic shape at the first eigenfrequency is no longer seen. Especially at the location of the point load, the amplitudes enlarged. With an asymmetric load, the amplitude over the length also becomes asymmetric, with the amplitude at the point load clearly being higher.

Weight

The influence of the amount of weight added to the system requires another plot. In this figure, the magnitude of all six peaks is visible along the length of the beam. These magnitudes are shown for all of the studied loads at PLL 3. This plot is given in figure 5.16.

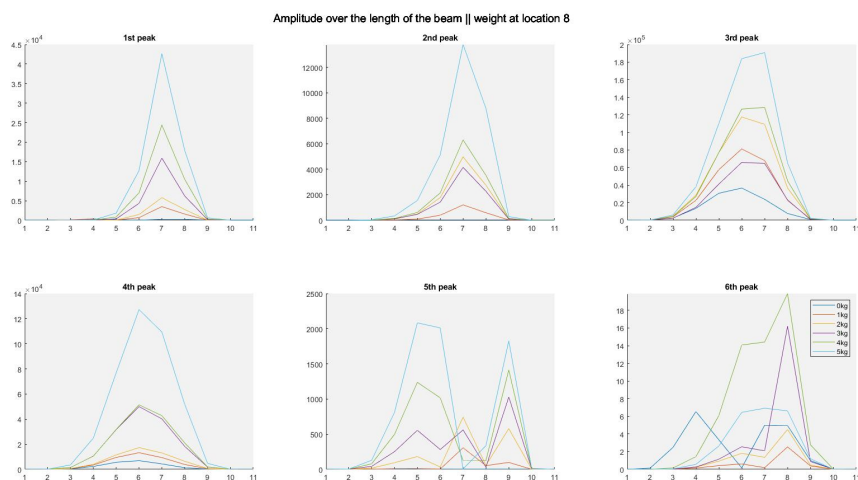


Figure 5.16: Behaviour of the amplitude over the length of the beam, with an increasing weight

The first thing to notice from the plots provided in figure 5.16 is that the shapes are very similar. Besides the sixth peak, the increase in weight enlarges the peak heights at all locations. The heights of the peaks, are given in table 5.5.

Location 6	0kg	1kg	2kg	3kg	4kg	5kg
1st peak	9.1	679.8	1471	4327	7018	12680
2nd peak	0	398.5	1423	1783	2152	5130
3rd peak	36640	65860	81200	117500	126600	183900
4th peak	6916	13280	17290	49990	51400	127200
5th peak	1.113	4.3	33.7	282.1	1017	2012
6th peak	0	0.6	1.8	2.56	14.1	6.5

Table 5.5: Influence of the weight on the magnitudes of the peaks in the Fourier analysis of the Energy Flux through location 6.

5.1.4. TIME-FREQUENCY-DOMAIN

Besides changes in frequencies over the length of the beam, we can also analyze changes over time. This requires another sort of analysis, known as a wavelet analysis. This will track what happens with the Fourier analysis over time. Since now we have 3 different entities to plot. This will be a 3D-plot. The color intensity can be seen as the height of the peak in the Fourier analysis. Some of the changes that were seen are discussed below. All figures are shown in the Appendix. An example of what these plots like is given below.

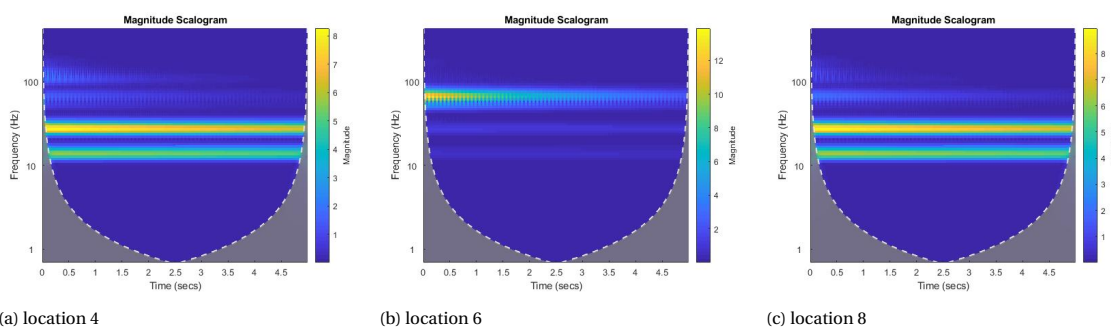


Figure 5.17: Wavelet analyses without any weights

You can look at these changes in multiple ways. When looking at a single wavelet analysis, they are not distinguishable. A slow decrease of intensity over time can be seen on every wavelet. However, not every frequency shows this decrease. When looking at the figures above, the lower frequencies do not seem to decrease amplitude, unlike the higher frequencies, that do decrease intensity rather quickly. The higher frequencies hold more energy within them and are therefore decreased faster. The dissipated energy mostly belongs to the higher frequencies.

The ripple effect you see at certain frequencies is due to how this specific wavelet analysis works. The wavelet is completely made up of a sinusoid, which means that in the signal, it fluctuates between being in and out of phase. This causes the maxima and minima visible in figure 5.17. At the lower frequencies, the temporal resolution is not high enough for the ripples to be visible. When another type of wavelet is used, these ripples are no longer visible.

5.2. DESIGN OF EXPERIMENT

Using the building blocks described in section 4.2, the final design for the experiment is made. This experiment was designed to be performed at the TU Delft¹. In this section, first the design is discussed by specifying the placement and uses for all measurement devices. Secondly, the expected outcome of the design is discussed.

5.2.1. FINAL DESIGN

In the experiment, the Energy Flux will be measured through two cross-sections. One in the middle, at the peak of the first eigenmode, and one at around three quarters the length of the beam, at one of the peaks of the second eigenmode. The locations match the antinodes of the first two eigenmodes. These locations were chosen, because of their behaviour in the numerical analysis. At these locations, the behaviour showed the biggest decency on the presence of a contact point.

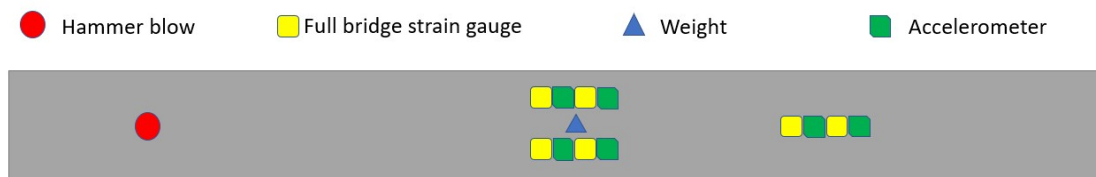


Figure 5.18: Top view of the experiment set-up

As discussed in section 2.4.1, the equation to measure Energy Flux in experiments slightly differs from the one used in the numerical analysis. The way the moment and the rotational velocity can be calculated have already been discussed. In the experiments, the following question should be answered:

- Can Energy Flux be measured experimentally?
- Are the results of these measurements comparable to the results of the numerical analysis?
- Can a vibrating beam be modeled in 1D?
- What is the influence of a contact area?

The moment can be calculated using a full bridge of strain gauges. When applied on multiple locations, Euler Bernoulli Beam Theory can be tested. The strains should be the same on both sides. If this indeed is the case, the neutral axis is assumed to be in the middle. This will provide us with the moment at that location. With the possibility to measure moments and rotational velocities, the Energy Flux can be calculated at any location.

5.2.2. EXPECTED RESULTS OF THE EXPERIMENT

Besides a direct extraction of the relevant quantities from ANSYS. The numerical analysis has also been done, using the same extraction method as the experiment. This way, a better comparison can be made between the experimental and the numerical results. The results from that analysis are discussed in Appendix A.

For the strain gauges to properly work, a minimal amount of strain is required, as discussed in section 4.1. The numerical model can give a good approximation of the expected strain. According to the model, the strains that will occur are $7 \cdot 10^{-5}$. The strain gauges to be used, can measure strains of $2 \cdot 10^{-6}m$ and higher. This means that, according to the numerical model, the strains will easily be large enough for the strain gauges to measure them.

¹This experiment was designed to be carried out in the Delft University of Technology - Stevin Laboratory 1. Therefore, the described measurement techniques and experiment requisites depended on the availability of the Stevin Lab. When executing this experiment in a different laboratory, adjustments to the material list and the design might be necessary.

5.2.3. FOLLOW UP EXPERIMENTS

The experiment described above will act as a proof of concept, and more experiments will have to be conducted before the technique can be applied in a slip-joint. The follow up experiments will first have to focus on the energy flux in a conical shaped structure. This could lead so significant changes. Secondly, other frequencies will have to be examined. Smaller contact areas can not be detected, if the wavelength of the eigenmode is too large. Acoustic wave, or ultrasonic wave measurements should be examined. These experiments should lead to a possible implementation of this technique in a slip-joint.

6

DISCUSSION

6.1. INTERPRETATION OF THE RESULTS

The results shown in chapter 5 are discussed below, which consists of an interpretation of the results in the time-domain and in the frequency-domain. The time-frequency-domain is not further discussed here.

6.1.1. TIME-DOMAIN

In the time-domain the amplitude of the Energy Flux and the Cumulative Energy Flux were studied over time. First of all, the course of the amplitude of the Energy Flux is discussed. The Energy Flux showed an increase of amplitude at the location of the contact point. However, the increase seen in figure 5.5, is expected to largely be caused by the incorrect effects of a point load in a numerical model. When the point load was located slightly next to a measurement location, these increases were less severe. This makes it unlikely, that a contact area can be identified by solely looking at an increase of amplitude. At points around the contact area, the EF also increased relative to the situation without a contact point.

Secondly, the Cumulative Energy Flux results were studied as well. The CEF showed a clear movement of energy towards the middle, at the side of the hammer blow. It could be theorized that right after the hammer blow, the energy density at this part of the beam is very high. This could explain the movement of the energy towards the other regions of the beam. A contact area had relatively little influence on this effect. A contact area can therefore be hard to detect using this information.

6.1.2. FREQUENCY-DOMAIN

Besides the time-domain, also the frequency-domain was analyzed. The interpretation of the Fourier analysis by studying the frequencies in the signal. At the exact location of the weight, the Fourier analyses showed more peaks than at any other locations. It would be interesting to see if the physical experiment shows the same effect. If so, this could be used for the detection of contact areas. However, it could also be a numerical error. A point load in a numerical model, is a force applied at a single infinitesimal point in the model. This can produce incorrect results, as was seen in the CEF plots in the time-domain.

Most of the frequencies in the signals were as expected. Only at the higher frequencies, the system deviated from the predicted behaviour. Although these deviations and the heights of the deviating peaks were small, they were consistent. However, when a point load was present, these divergences were no longer prevailed. The reason for the deviating peaks is unknown.

Surprisingly, PLL 1 and the other PLL's showed, to some extent, different results. The locations of the peaks differed. At PLL 1, the same locations were found as without weight, whereas at the other PLL's, the peaks were found at the expected locations. This would indicate that the surprising peaks depend on the second eigenfrequency, because PLL 1 had no influence on the second eigenfrequency.

6.2. DIFFERENCE BETWEEN THE TWO ENERGY FLUX EQUATIONS

This thesis uses two equations to calculate Energy Flux

$$\mathbf{S} = -M \cdot \dot{w}' + V \cdot \dot{w} \quad (6.1)$$

$$\mathbf{S} = 2M \cdot \dot{w}' \quad (6.2)$$

The situation for which it was proven that these two are equal, uses an infinite beam. That beam has no reflection of energy, as all energy only passes each cross-section once. Which is a large part of the energy flowing through the system examined in this study. In the actual slip-joint, this is expected to be less.

6.3. VALIDITY OF THE MODEL

Energy Balance

One way to check the validity of the model is to check the energy balance. From the derivation of the Energy Flux equation in section 2.4 it is known that:

$$\frac{d\mathbf{S}}{dx} = \frac{dE}{dt} \quad (6.3)$$

In other words, this means that the change in Energy Flux over the length of the beam must equal the change of stored energy in that part of the beam, over time. For the model, this equation has to hold. The first part, $d\mathbf{S}/dx$, is calculated using Energy Flux calculations on two parts of the beam, close to each other. The difference between the two, divided over the distance between them, results in this first term. For the second term, three types of energy storage had to be calculated: kinetic energy, deformation energy, and height energy. These quantities were calculated using the following equations:

$$E_k = \frac{1}{2}mv^2 \quad (6.4)$$

$$E_b = \frac{1}{2}EI\kappa^2 \quad (6.5)$$

$$E_h = mgh \quad (6.6)$$

The total amount of stored energy is the sum of the quantities above. Now, both sides of equation 6.3 can be plotted. These should show the same results, as can be seen in figure 6.1. Only in the first 50 milliseconds, a difference between the two can be seen. At these time steps, energy was still being put into the system.

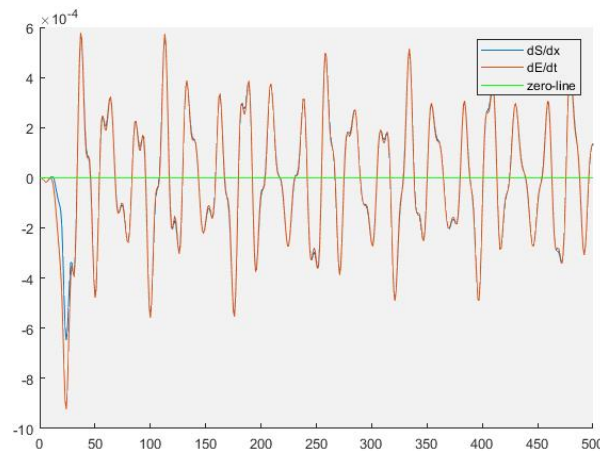


Figure 6.1: The change in stored energy over time, and the change in Energy Flux over x.

Eigenfrequencies

Another way of validating the model is by analytically calculating the eigenfrequencies, and comparing those with the eigenfrequencies calculated by the model. Using the method described in section 2.3.3 the eigenfrequencies were calculated, results can be found in table 6.1. This table shows that the analytically calculated eigenfrequencies are the same as the numerically calculated eigenfrequencies.

The first natural frequency is given by:

$$\omega_n = C \cdot \sqrt{\frac{EI}{\rho AL^4}} = 9.87 \cdot \sqrt{\frac{360}{7850 \cdot 0.0006 \cdot 1^4}} = 86.29 \frac{rad}{s} \quad (6.7)$$

with $\rho = 7850 kg/m^3$, $A = 0.006 \cdot 0.1 = 0.0006 m^2$ and $L = 1 m$. λ is the wavelength of the mode and $\lambda L = \pi$

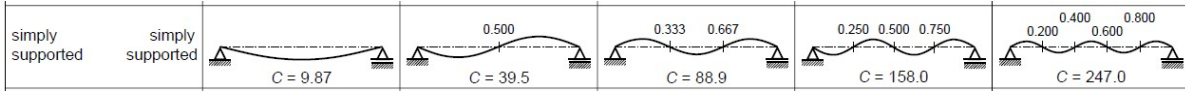


Figure 6.2: C values for simply supported beams, as found in (Spijkers et al., 2005a)

This gives us a first natural frequency of

$$f = \frac{\omega}{2\pi} = 13.73 \text{ Hertz} \quad (6.8)$$

Natural Frequencies	First	Second	Third	Fourth	Fifth
Analytical $f[Hz]$	13.7	54.96	123.70	219.85	343.7
Numerical $f[Hz]$	13.732	54.918	123.53	219.51	342.8

Table 6.1: The calculated analytical eigenfrequencies of the system

The differences between the numerically and the analytically calculated natural frequencies are within 0.003%. This confirms the numerical model to be correct.

6.4. APPLICATION IN THE SLIP-JOINT

Now that the behaviour of Energy Flux is more properly understood, a real-life application can be discussed. The situation in the slip-joint connection is very different than in the proposed experiment and the numerical model. However, the results show possible implementations in a slip-joint connection. There are two main possibilities for such an implementation, excitement of the global eigenmodes, and excitement of the local eigenmodes. Both possibilities are discussed below.

Global eigenmodes

The global eigenmodes are already excited during installation. These eigenmodes, and their corresponding eigenfrequencies are seen in figure 6.3. From the results of this thesis, it is expected that the behaviour of the Energy Flux will depend on contact points. The results showed that at certain locations of an eigenmode, no Energy Flux is transported in the corresponding eigenfrequency. However, with the presence of a contact point, this transport does occur in that eigenfrequency. This phenomenon could be used to detect the locations of contact points using the global eigenmodes method.

However, there is one limitation of the global eigenmodes method. During installation, the system is excited in one eigenfrequency at a time. This complicates the implementation of the Energy Flux method, because the results of the frequency-domain presented in section 5.1.3 show that the presence of multiple eigenfrequencies in the behaviour is essential. This is because the relative importance of an eigenfrequency provides information about the locations of contact points. However, it is expected that there is only one eigenfrequency present during the harmonic load of the installation.

Therefore, the global eigenmodes method cannot be used during installation. An alternative would be to excite the system with a single impulse, forcing free vibration.

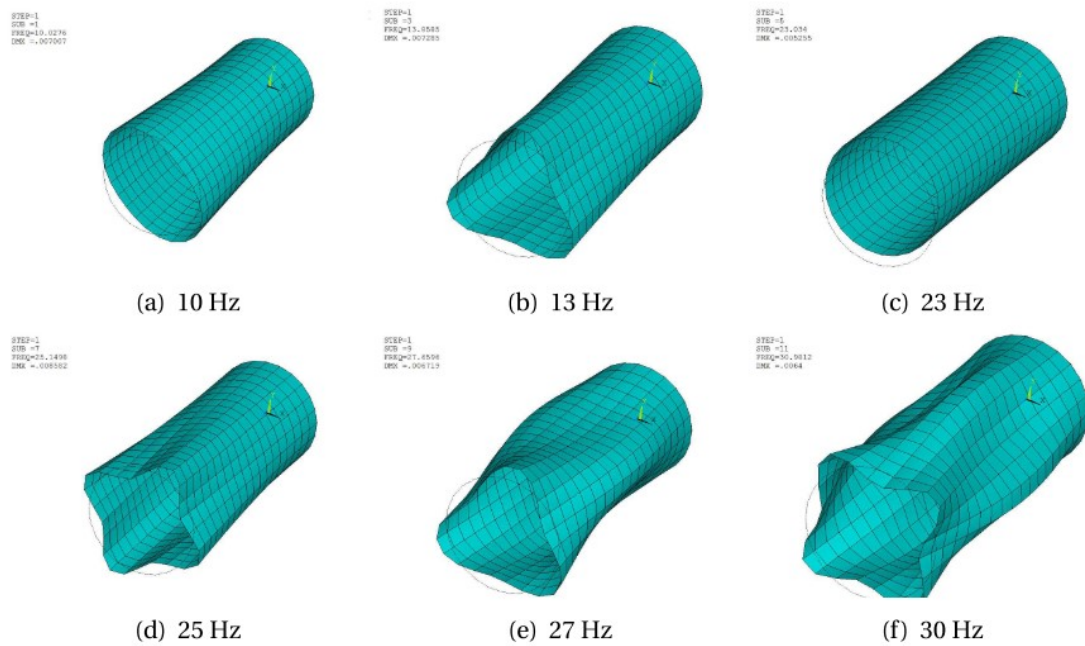


Figure 6.3: Global Mode Shapes, as found by (Segeren, 2017)

Local eigenmodes

Contrary to the global eigenmodes method, for the local eigenmodes approach only a small part of the entire connection will vibrate. For this method, the exciting force is applied at one specific location. In this method, only a very small part of the connection can be examined each time. This means that the wavelength of the eigenmodes should also decrease, excitation should be done in much higher frequencies.

The excitement of local eigenmodes is more closely comparable to the analysis done in this thesis. The contact-less, or 'free' areas in the slip-joint, will in this case form the span of the beam in the experiment. The high pressure contact areas surrounding the free area could act as the supports in the experiment. The detecting of contact areas works the same as it did in the numerical analysis performed in this study. For this method, the importance of the eigenfrequencies can be compared. This information could be used to find the location of contact points.

However, while this method seems promising, several aspects need further research. Recommendations for this can be found in section 7.2

7

CONCLUSIONS AND RECOMMENDATIONS

7.1. KEY FINDINGS

In this thesis, the application of the Energy Flux method for the detection of contact areas has been researched. In this section the key findings for answering the research questions are listed. First the two sub-questions will be answered, after which the main research question will be discussed.

What is the influence of a contact point on Energy Flux in the time-domain, frequency-domain and time-frequency-domain?

For this research question, the behaviour of EF was examined both with and without a contact point. First the general behaviour of EF in a vibrating beam was examined. It was found that:

- For short beams $\mathbf{S} = -M \cdot \dot{w}' + V \cdot \dot{w}$ should be used, because the Energy Flux equation $\mathbf{S} = 2 \cdot M \cdot \dot{w}'$ does not apply. However, in a slip-joint the latter equation may still be valid.
- Close to the location of energy input, the energy moves towards the longer, unsupported section of the beam. This results in a more evenly spread energy density.

Now that the general behaviour of EF in a vibrating beam is known, the influence of a contact point can be studied. For those it was found that:

- The influence of contact areas is most pronounced in the frequency-domain. The presence and location of a contact area had little influence in the time- and time-frequency-domain.
- In the frequency domain it can be seen that the presence of a contact point introduces two new frequencies in the EF signal, namely twice the first and twice the second eigenfrequencies.
- In the studied domains, the exact location of an introduced contact point is difficult to identify. However, an estimate of the location was easily found, because the changes of the frequencies within the EF were most pronounced around the contact point.

How can the numerical results be validated in an experiment?

The numerical results are promising and show that, especially in the frequency-domain the presence of a contact point can be indicated. In this study an experiment was proposed, which should validate the numerical findings. This experiment measures the EF through two cross-sections of a vibrating simply supported beam. The two cross-section are located at the antinodes of the first two eigenmodes. These locations were chosen, because the numerical results indicated the largest difference in behaviour at those points. An overview of the experiment set-up can be seen in figure 3.1.

How can the Energy Flux method be used to detect contact areas in a vibrating steel beam?

Based on these sub-questions the main research question can be answered. The question has been approached from two sides, numerically and experimentally.

Numerically, the frequency-domain is the best indicator of a contact point. Although the exact location is difficult to find, the presence and the approximate location of a contact point can be determined.

Experimentally, the EF can be calculated by measuring strains and accelerations at two points besides one another. The numerical results indicate that the presence of a contact point will introduce two new frequencies in the EF.

7.2. SUGGESTIONS FOR FURTHER RESEARCH

Even though the results of this thesis are promising for the application of the Energy Flux method for the detection of contact areas in a slip-joint connection, a real-life implementation is still a long way out. Further research is needed on the following aspects:

- It should be studied whether the EBBT is applicable in a cylindrical shape. Several of the assumptions made in EBBT, could be invalid in a slip-joint, such as the absence of the shear deformation, and of the rotational inertia. This could be studied by performing a similar experiment, both numerical as experimental, as conducted in this study on a cylinder, instead of a beam.
- In this study the numerical results of the two Energy Flux equations were different. The numerical results showed that $\mathbf{S} = M \cdot \dot{w}'$ is not valid in a beam. It should be studied whether this equation is valid in a cylinder. Because a cylinder more closely resembles the situation for which the two equations are identical, this is promising.
- The orthogonal component of a contact area is not taken into account in this study. Even though the influence of this component is expected to be small, further research is needed to confirm this.
- In-field measurements of strains and accelerations during the slip-joint installation should be studied. The frequencies within these signals and their corresponding locations will show the potentials of the global eigenmodes method.



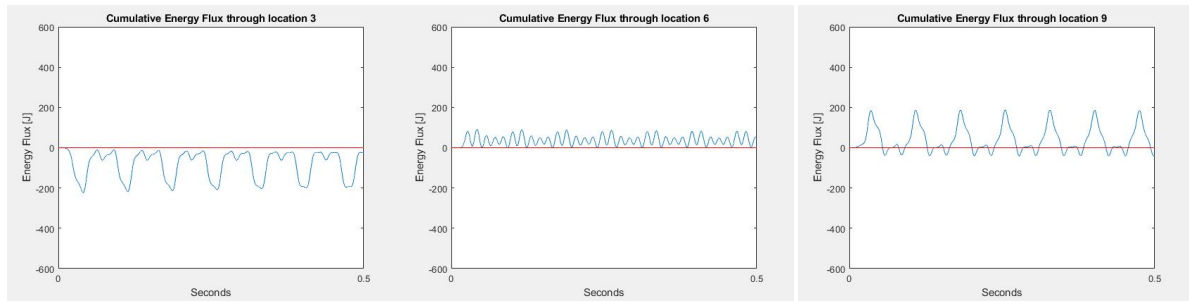
EXPECTED EXPERIMENT RESULTS

Besides a direct extraction of the relevant quantities from ANSYS. The numerical analysis has also been done, using the same extraction method as the experiment. This way, a better comparison can be made between the experimental and the numerical results. The results of this analysis are discussed here.

The expected results for the experiment differ from the results of the numerical model, because the equation with which the Energy Flux is calculated differs, see sections 2.4.1. For a quick evaluation of the experimental results, the experimental equation has also been put into the numerical model, in this subsection, those results are discussed.

As discussed earlier, Energy Flux is a vector. When plotted over time, the direction is given by the sign of the scalar (above or below 0). All values above zero indicate an Energy Flux in a positive direction, in this case to the right. Values below zero indicate flux in the opposite direction, in this case leftward. When this signal is then integrated. The complete energy through this cross-section can be calculated. A cumulative integration would mean to subtract negative Energy Flux from the positive Flux. Again, this cumulative Energy Flux can be plotted. These plots can be roughly subdivided in three categories.

- **CEF through the left half of the beam, at the side of impact, see sub-figure A.1a.**
The net Energy Flux is always positive, meaning to the right. As the input of energy is at this side of the beam, this is not a surprising result. First, some of the energy input has to move rightwards, to get a more homogeneous distribution of energy. Once this is achieved. The CEF simply fluctuates. All CEF plots at this side of the beam qualitatively look like this.
- **CEF through the middle of the beam, see sub-figure A.1b.**
In the middle of the beam, the CEF looks slightly different. More centered, albeit still mostly positive. This can be explained by the fact that the hammer blow was on the left side. Naturally, more energy will then move rightwards through the middle. In Appendix A, a figure can be seen with the hammer blow on the other side.
- **CEF through the right half of the beam, see sub-figure A.1c.**
The right half of the beam looks more like the left, with the important difference that the CEF is not always positive. Unsurprisingly, the CEF is now mostly negative, meaning leftwards. It fluctuates around zero.



(a) CEF through location 3

(b) CEF through location 6

(c) CEF through location 9

Figure A.1: Cumulative Energy Flux through three locations, without added weight.

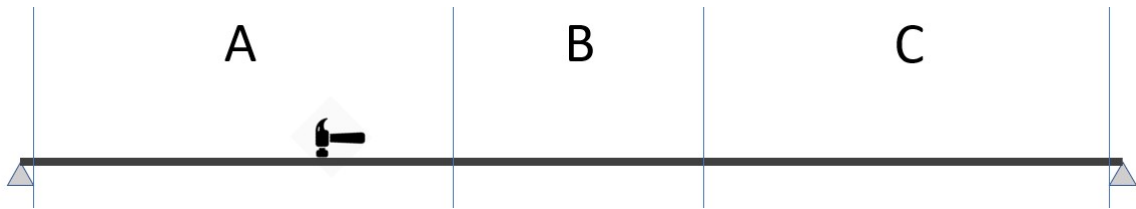


Figure A.2: Overview of the behaviour areas of the cumulative Energy Flux

In these figures, it becomes clear that the location of the weight influences the behaviour of the amplitudes. At the location of the weight, there is an increase in amplitude. The amplitude of the third peak remains low, but a small increase is visible at exactly the point of the weight. This peak becomes more apparent when the y-axis is not set. At the first eigenfrequency, the half with the weight is increased. A precise location is hard to pinpoint, but a general location can easily be found.

All expected results in the frequency-domain can be found below. For all PLL's, weights, locations and peaks, the height of the fourier analysis. Figure A.3 shows the height of the peaks for PLL 1, the first figure shows the height of the peaks at location 1. The colours indicate the amount of weight at the corresponding PLL. This way, all information is shown in one figure.

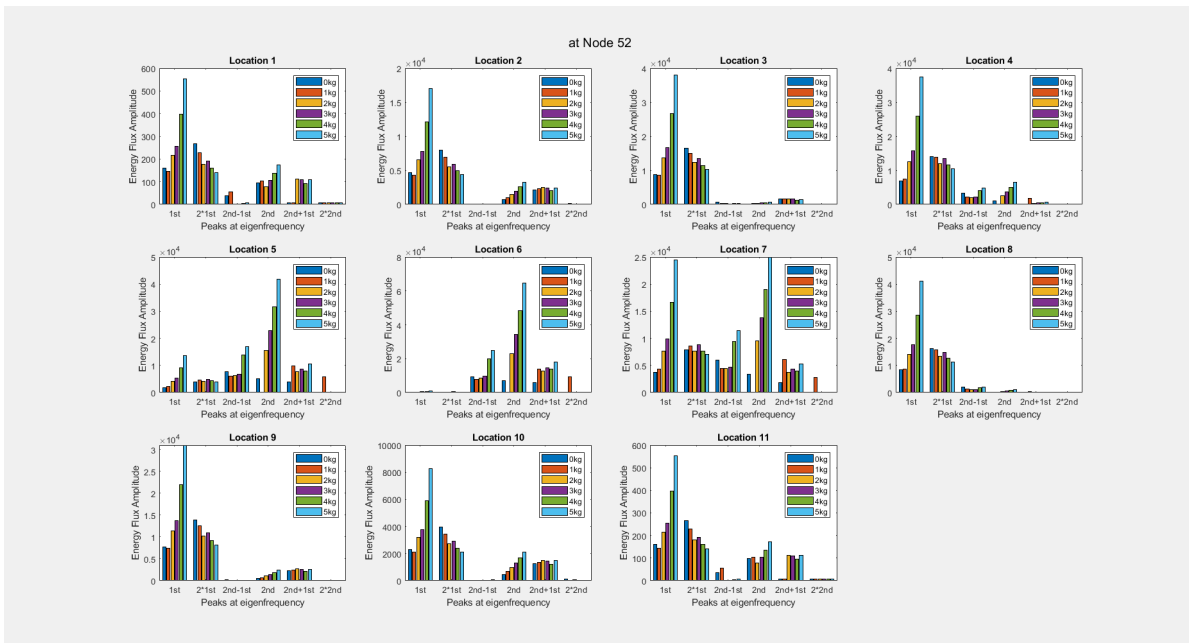


Figure A.3: The expected results of the experiment with PLL 1.

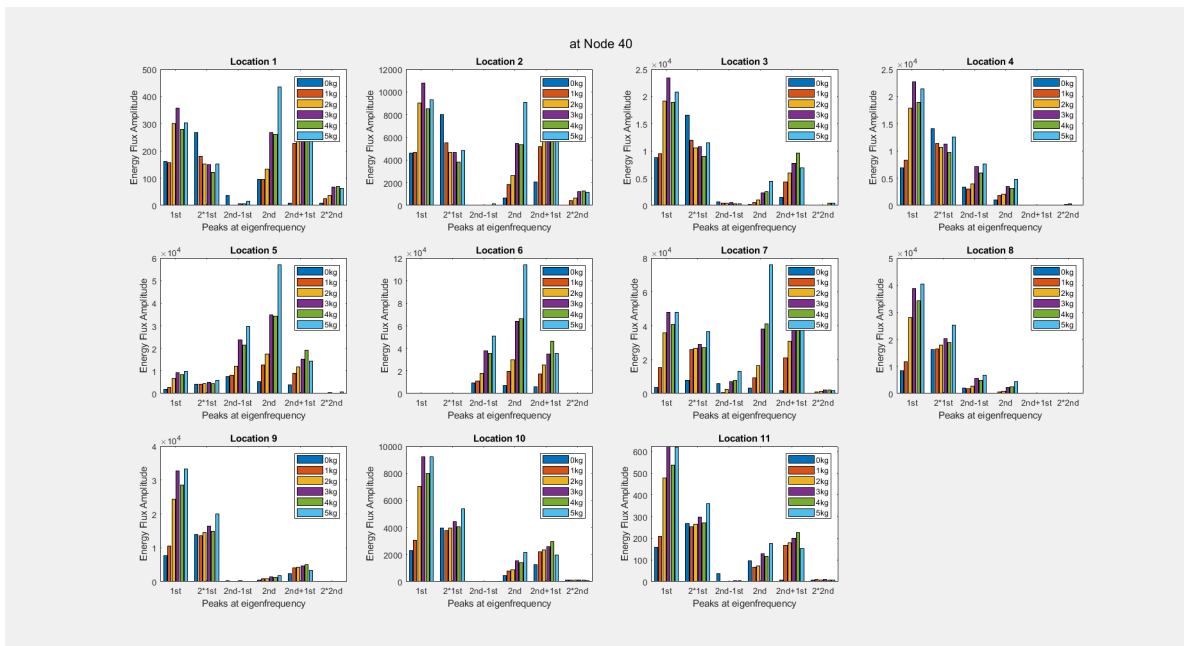


Figure A.4: The expected results of the experiment with PLL 2.

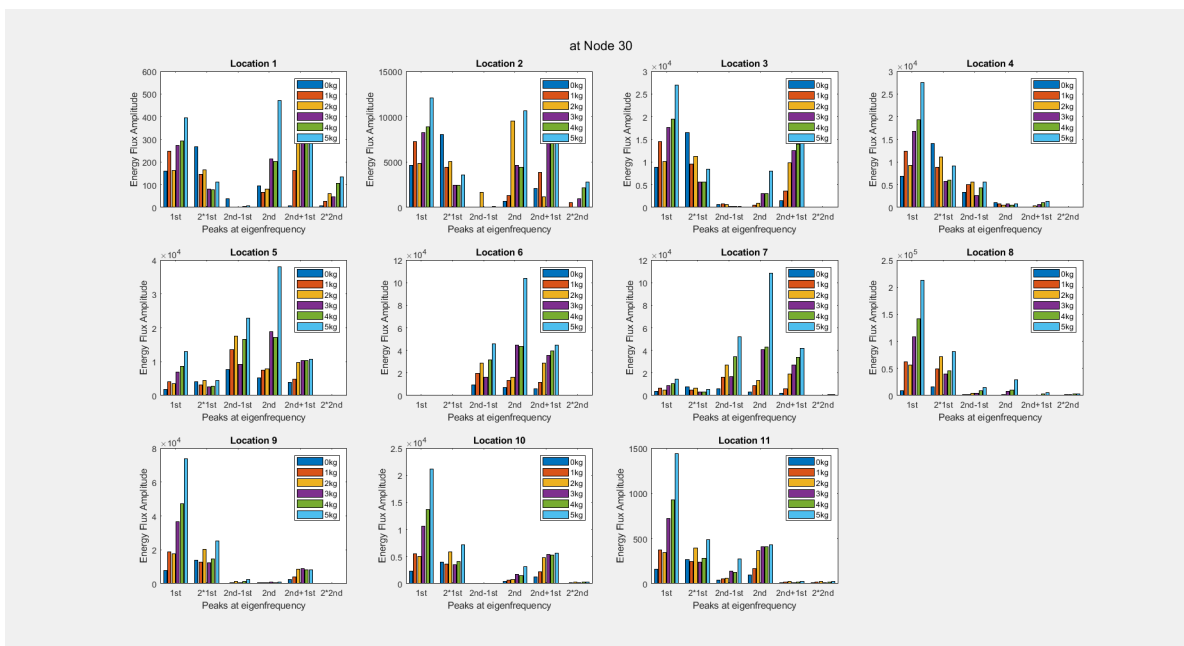


Figure A.5: The expected results of the experiment with PLL 3.

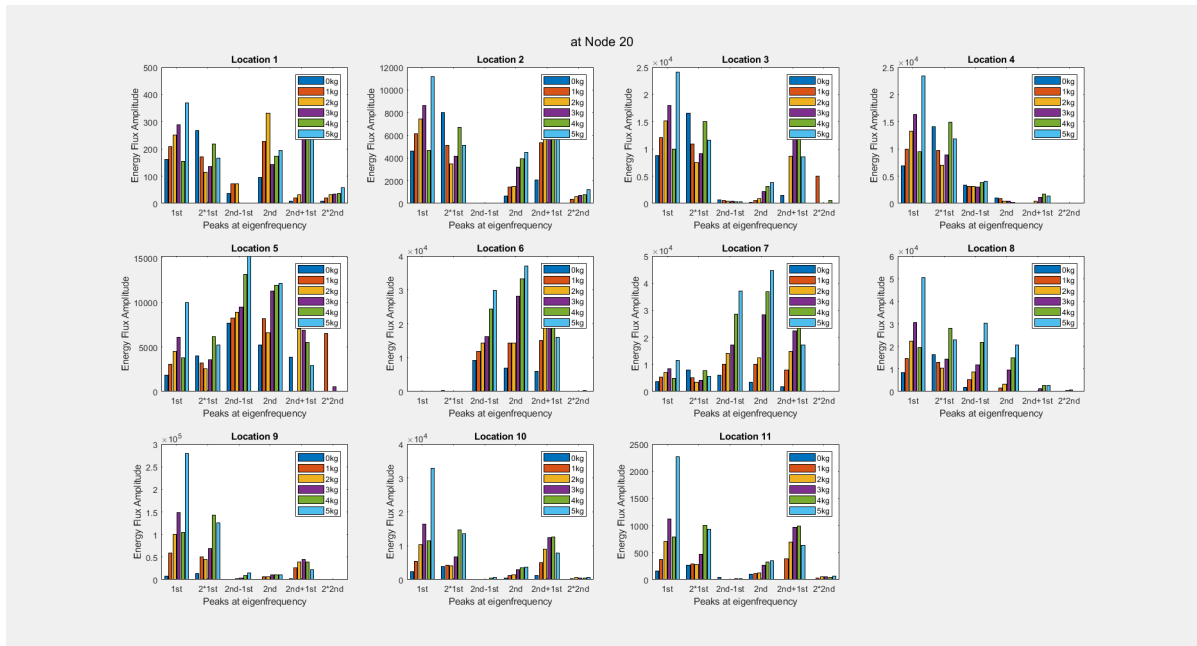


Figure A.6: The expected results of the experiment with PLL 4.

B

CUMULATIVE ENERGY FLUX RESULTS

As described in section 5.1.2, The cumulative energy flux results have been calculated for all systems. The results of those calculations are shown below for all systems that have been investigated.

B.1. PLL 1

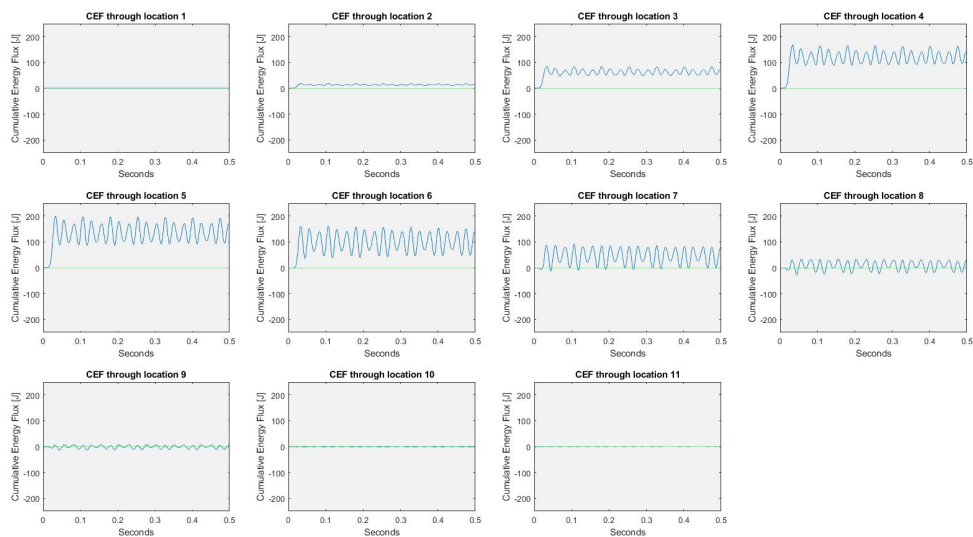


Figure B.1: CEF through all locations with 1 kilogram at PLL 1

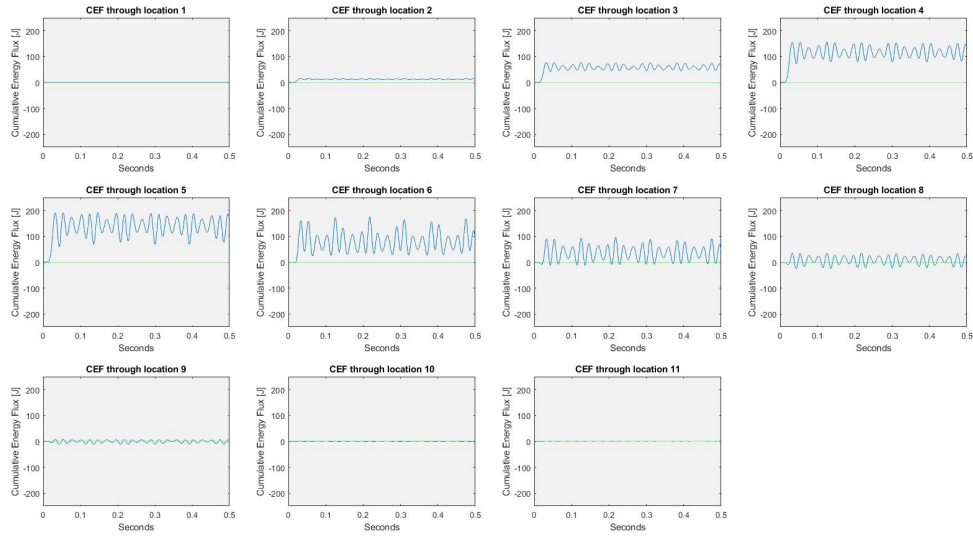


Figure B.2: CEF through all locations with 2 kilogram at PLL 1

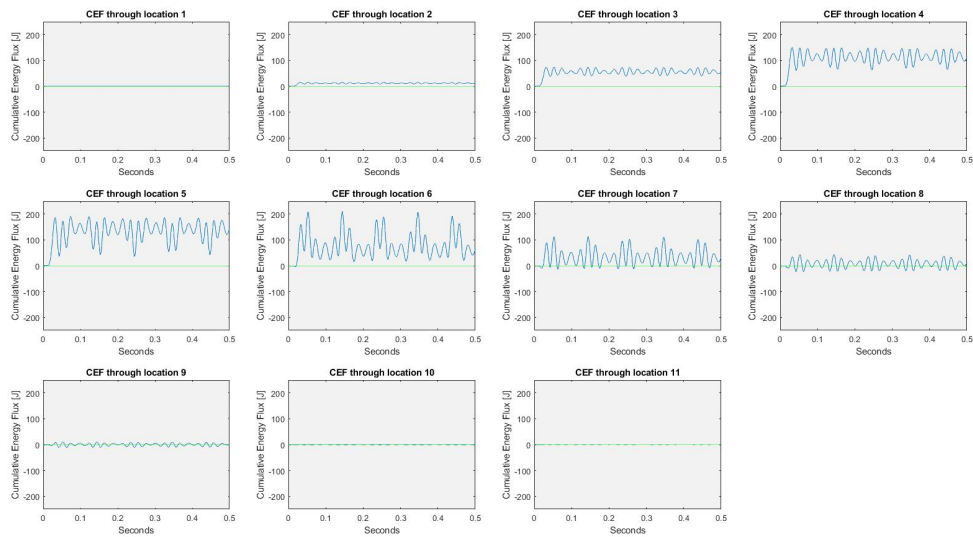


Figure B.3: CEF through all locations with 3 kilogram at PLL 1

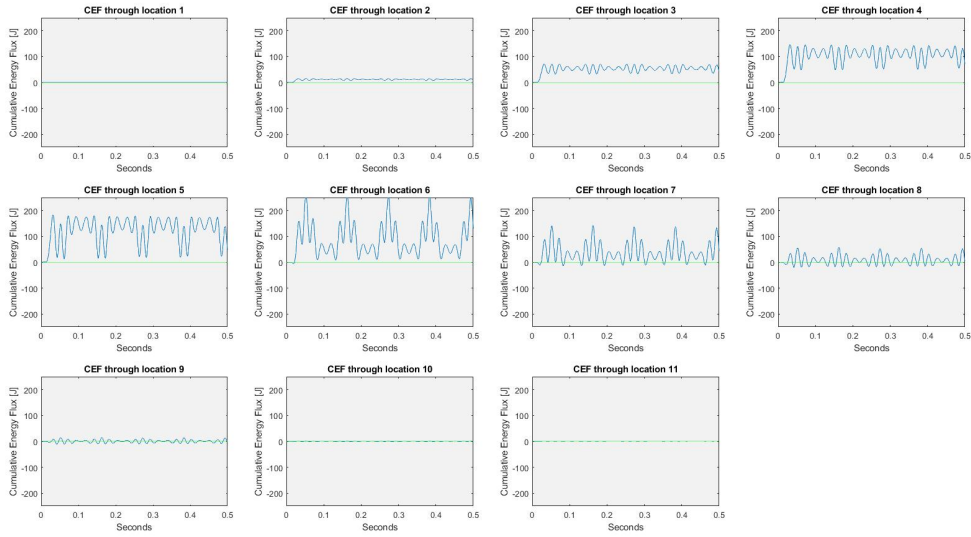


Figure B.4: CEF through all locations with 4 kilogram at PLL 1

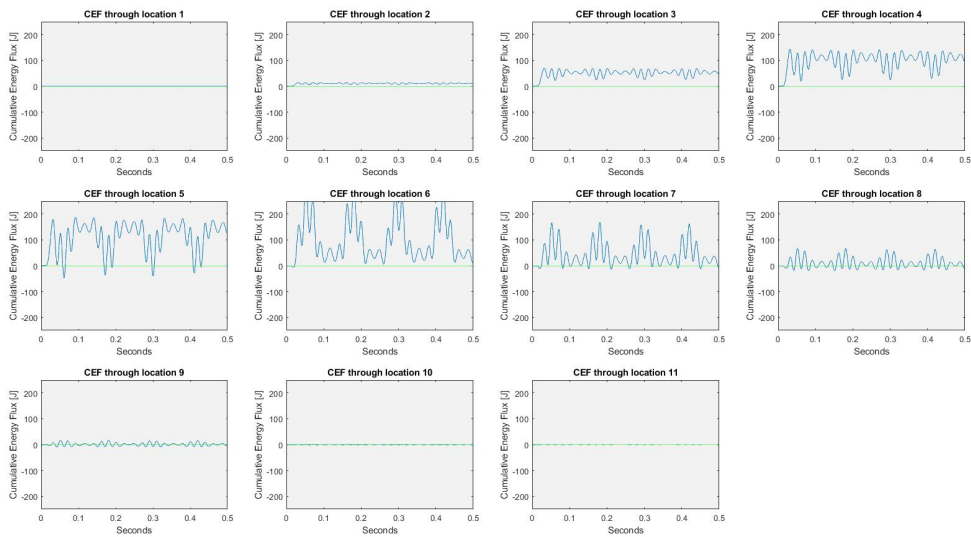


Figure B.5: CEF through all locations with 5 kilogram at PLL 1

B.2. PLL 2

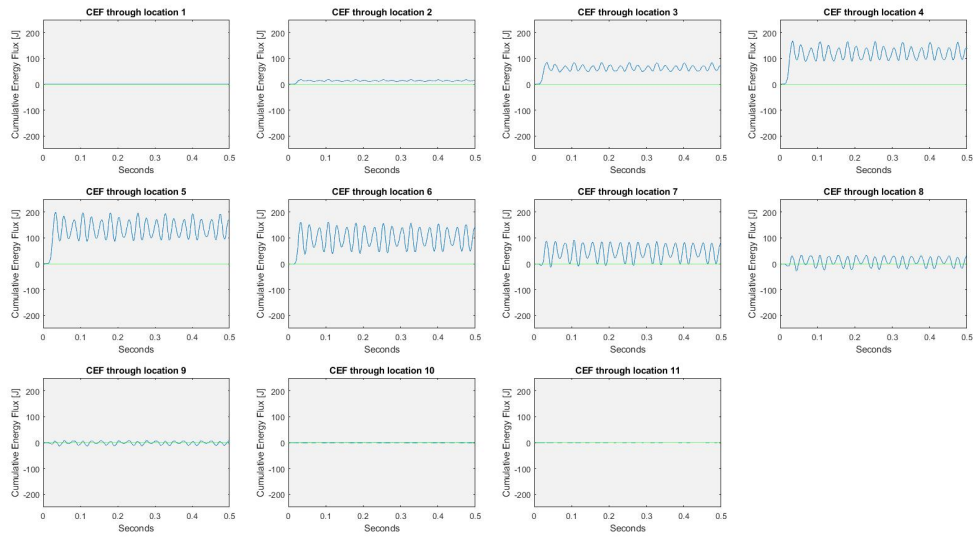


Figure B.6: CEF through all locations with 1 kilogram at PLL 2

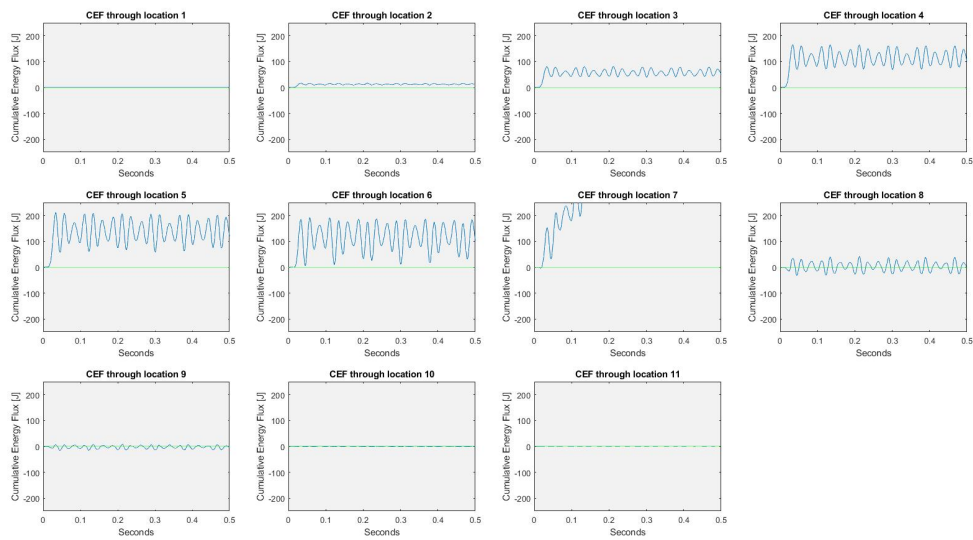


Figure B.7: CEF through all locations with 2 kilogram at PLL 2

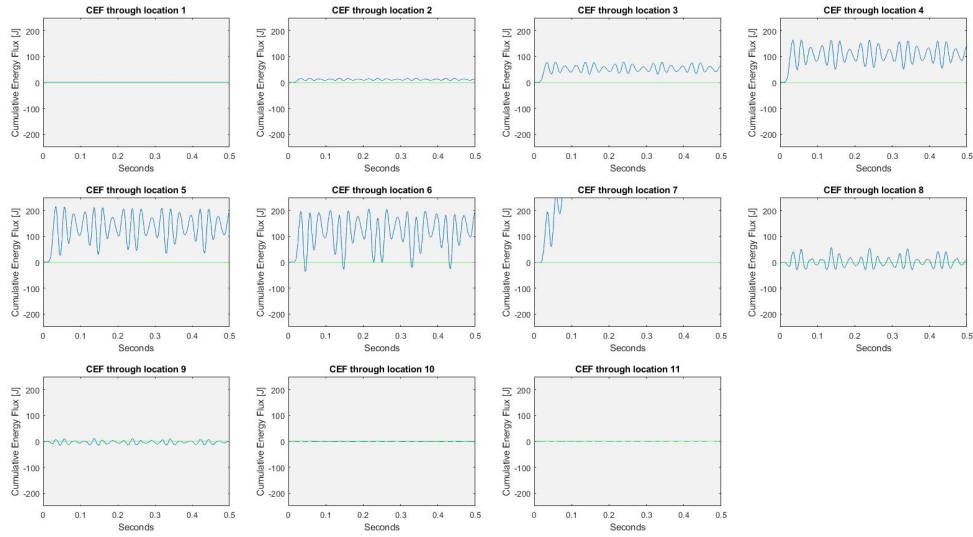


Figure B.8: CEF through all locations with 3 kilogram at PLL 2

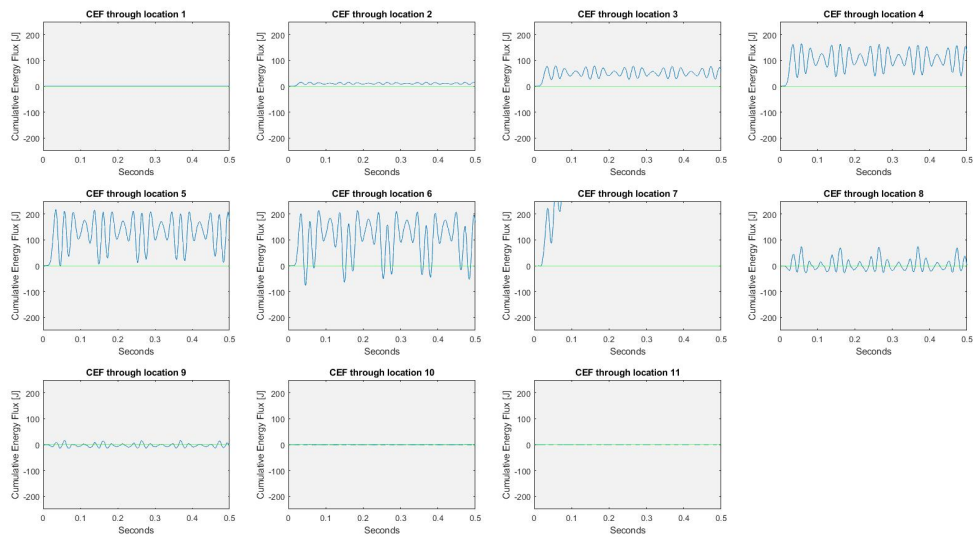


Figure B.9: CEF through all locations with 4 kilogram at PLL 2

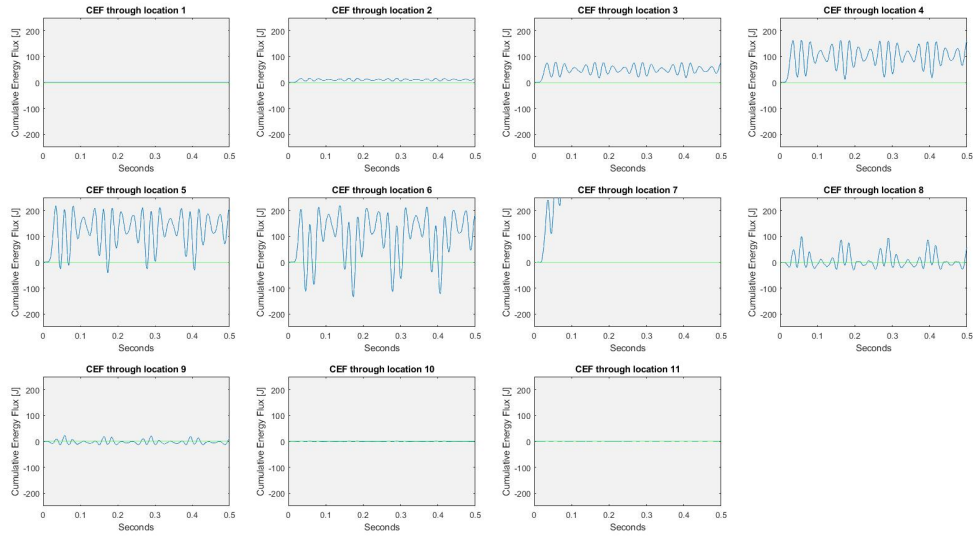


Figure B.10: CEF through all locations with 5 kilogram at PLL 2

B.3. PLL 3

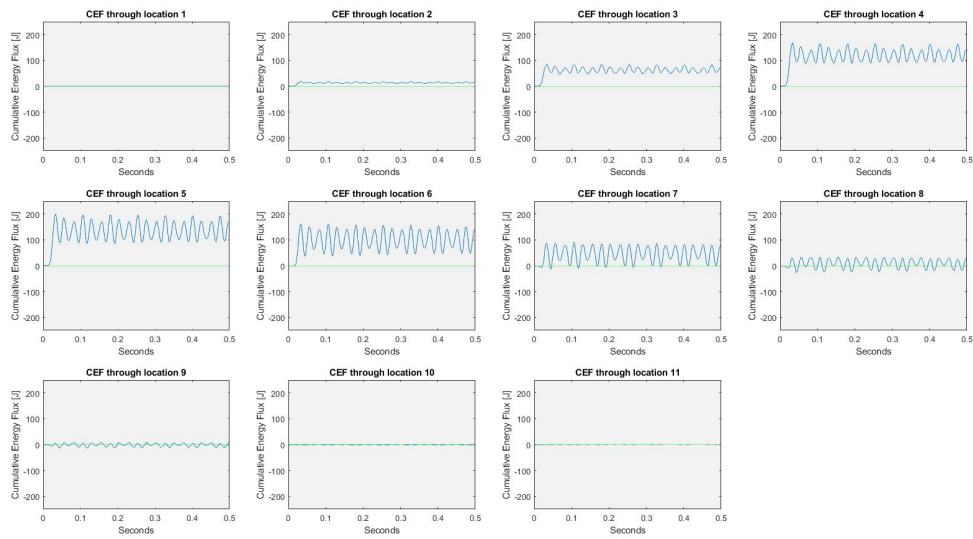


Figure B.11: CEF through all locations with 1 kilogram at PLL 3

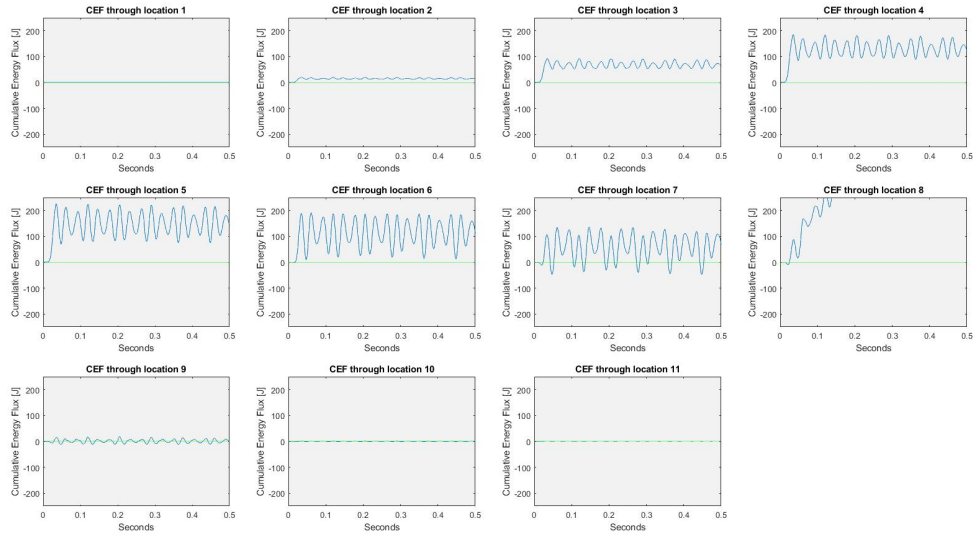


Figure B.12: CEF through all locations with 2 kilogram at PLL 3

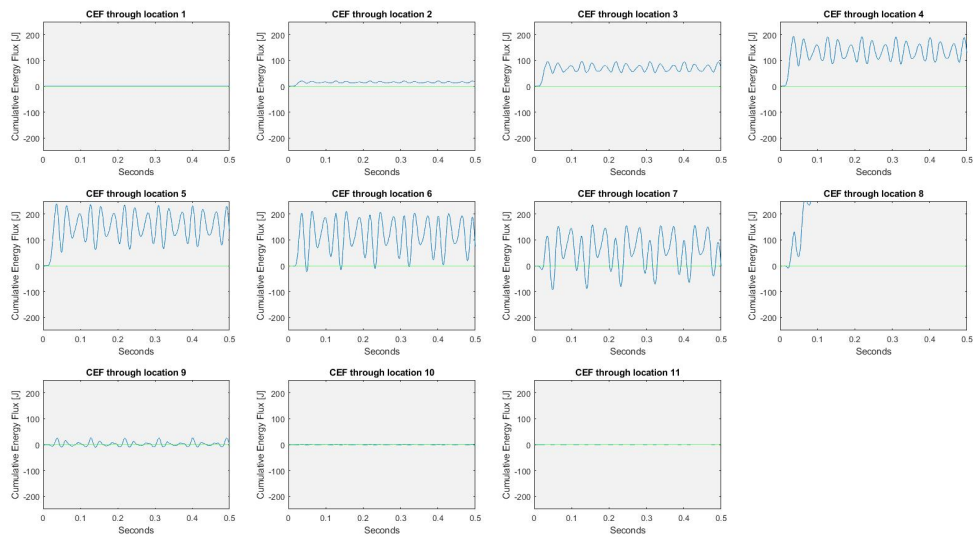


Figure B.13: CEF through all locations with 3 kilogram at PLL 3

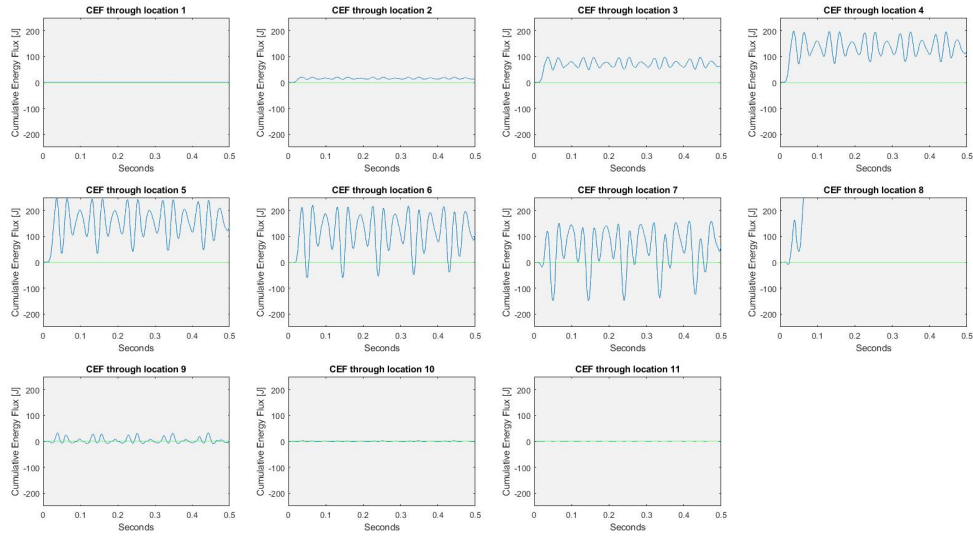


Figure B.14: CEF through all locations with 4 kilogram at PLL 3

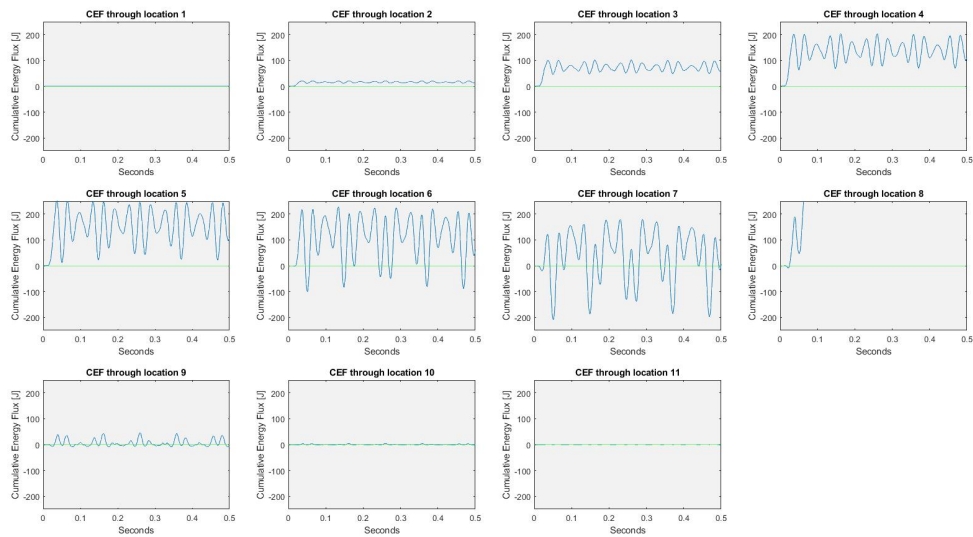


Figure B.15: CEF through all locations with 5 kilogram at PLL 3

B.4. PLL 4

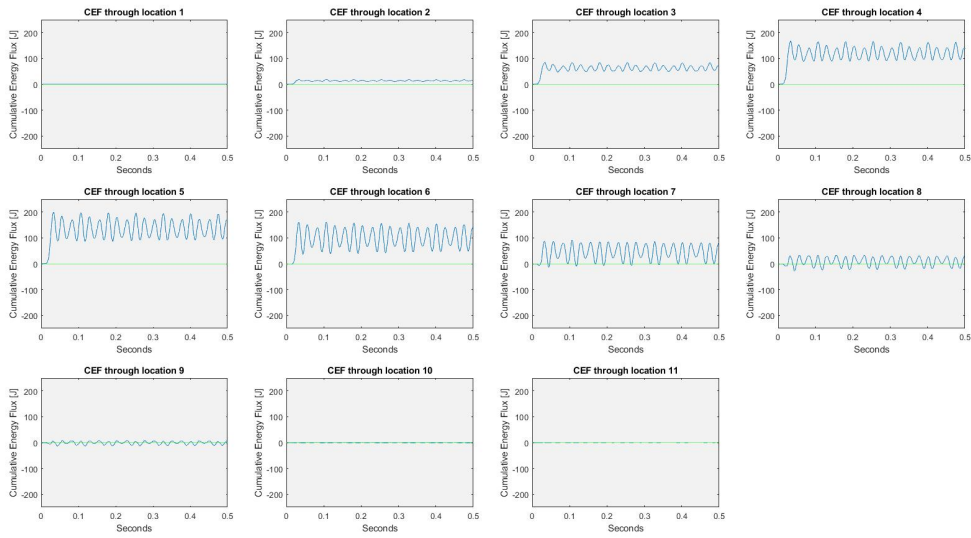


Figure B.16: CEF through all locations with 1 kilogram at PLL 4

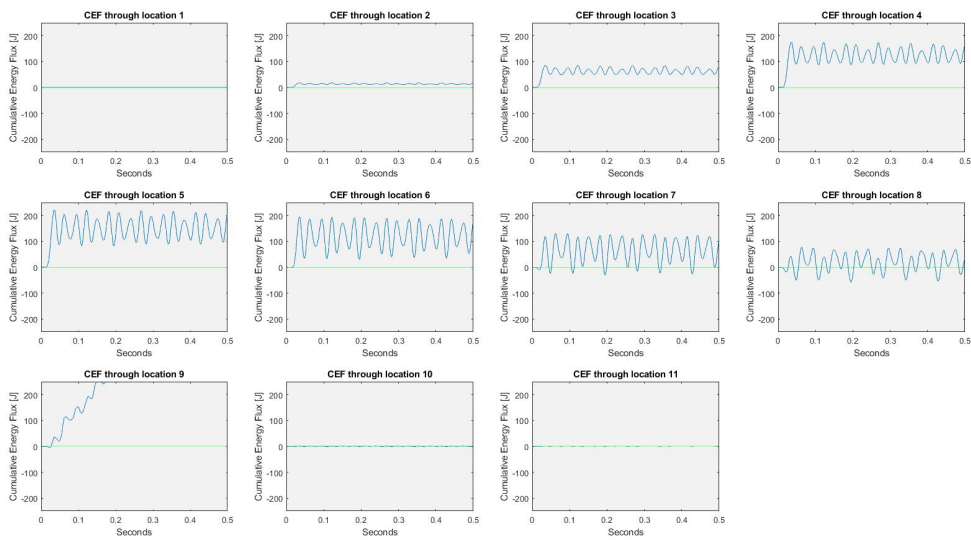


Figure B.17: CEF through all locations with 2 kilogram at PLL 4

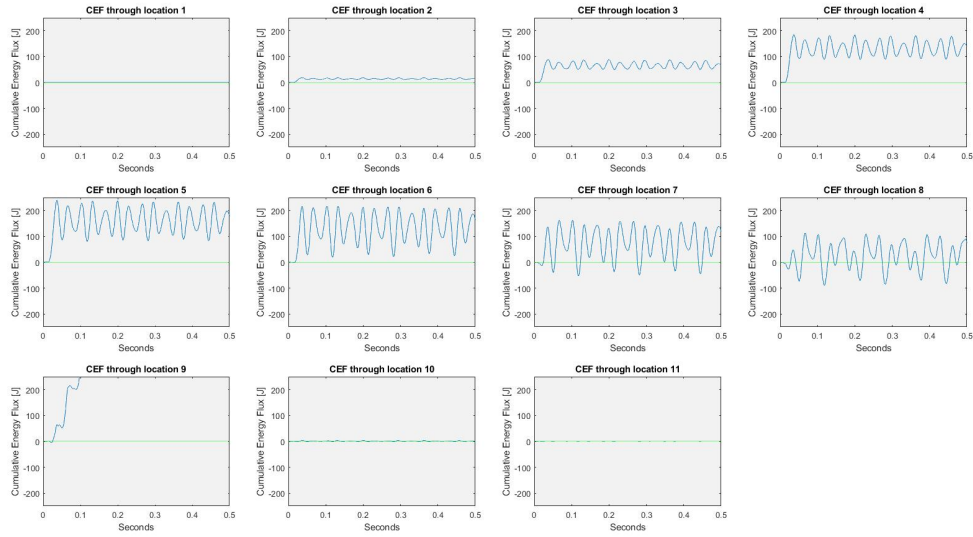


Figure B.18: CEF through all locations with 3 kilogram at PLL 4

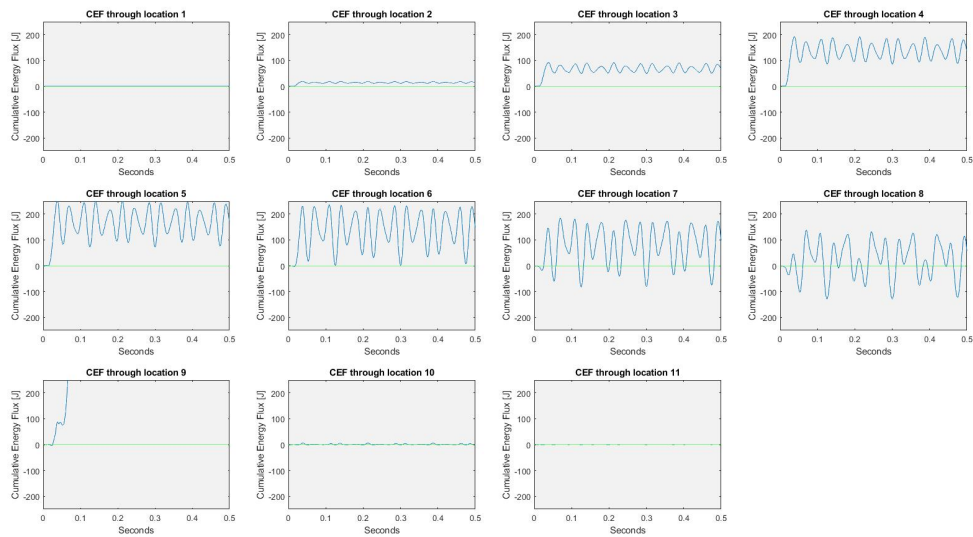


Figure B.19: CEF through all locations with 4 kilogram at PLL 4

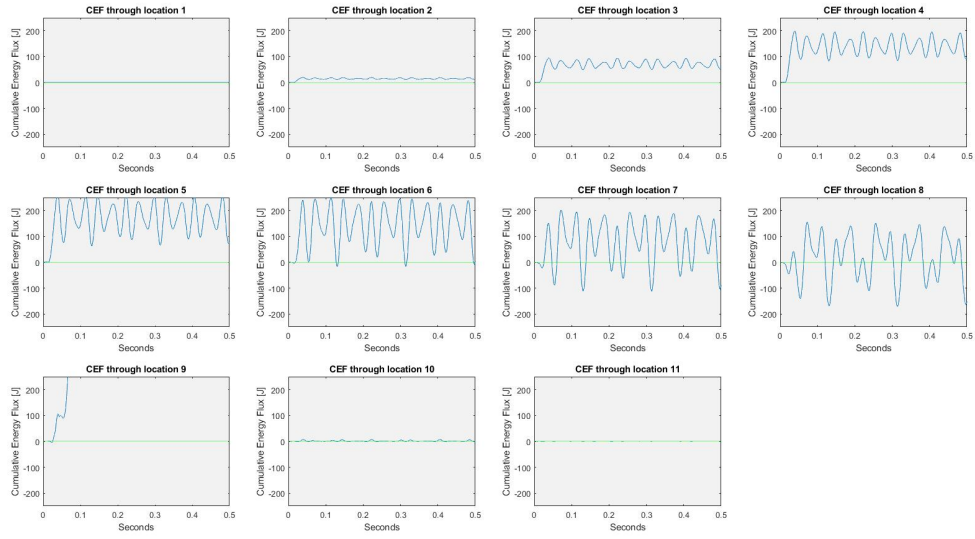


Figure B.20: CEF through all locations with 5 kilogram at PLL 4

BIBLIOGRAPHY

- Atkinson, R. (2018). A heat-transfer based method for slip-joint contact area measurement.
- Bauchau, O. A. and Craig, J. I. (2009). *Structural analysis: with applications to aerospace structures*, volume 163. Springer Science & Business Media.
- Department of applied Mechanics, Budapest University of Technology (2018). BEAM188 Element Description. [https://www.mm.bme.hu/~gyebro/files/ans_help_v182/ans_elem/Hlp_E_BEAM188.html#:~:text=BEAM188%20has%20six%20or%20seven,\(warping%20magnitude\)%20is%20optional.](https://www.mm.bme.hu/~gyebro/files/ans_help_v182/ans_elem/Hlp_E_BEAM188.html#:~:text=BEAM188%20has%20six%20or%20seven,(warping%20magnitude)%20is%20optional.) Accessed on 16.11.2020.
- Edenhofer, O., Pichs-Madruga, R., Sokona, Y., Seyboth, K., Kadner, S., Zwickel, T., Eickemeier, P., Hansen, G., Schlömer, S., von Stechow, C., et al. (2011). *Renewable energy sources and climate change mitigation: Special report of the intergovernmental panel on climate change*. Cambridge University Press.
- EWEA (European Wind Energy Association) (2013). Deep water: the next step for offshore wind energy. *Brussels, Belgium: A report by the European Wind Energy Association*.
- Graff, K. F. (2012). *Wave motion in elastic solids*. Courier Corporation.
- Kamphuis, T. (2016a). "dot500 slj - tse her 2016 - tehe115072 - eindrapportage_v14".
- Kamphuis, T. P. J. (2016b). *Design, testing and verification of the DOT500 slip- joint support structure*. PhD thesis.
- Komušanac, I. (2020). Wind energy in europe in 2019: Trends and statistics.
- Lee, Y.-S., González, J. A., Lee, J. H., Kim, Y. I., Park, K., and Han, S. (2016). Structural topology optimization of the transition piece for an offshore wind turbine with jacket foundation. *Renewable energy*, 85:1214–1225.
- Lotsberg, I. (2013). Structural mechanics for design of grouted connections in monopile wind turbine structures. *Marine structures*, 32:113–135.
- Lotsberg, I., Serednicki, A., Lervik, A., and Bertnes, H. (2012). Design of grouted connections for monopile offshore structures: results from two joint industry projects. *Stahlbau*, 81(9):695–704.
- Rao, S. S. (1995). Mechanical vibrations laboratory manual. *Edition Addison-Wesley Publishing Company, New York*.
- Sanchez Gomez, S. (2019). *Energy flux method for identification of damping in high-rise buildings subject to wind*.
- Segeren, M. (2017). *Vibration Induced Settlement of a Slip Joint Connection for Offshore Wind Turbines*. PhD thesis.
- Segeren, M. L., Lourens, E.-M., Tsouvalas, A., and Van Der Zee, T. J. (2014). Investigation of a slip joint connection between the monopile and the tower of an offshore wind turbine. *IET Renewable Power Generation*, 8(4):422–432.
- Shabana, A. A. and Ling, F. F. (1997). *Vibration of discrete and continuous systems*. Springer.
- Spijkers, J., Vrouwenvelder, A., and Klaver, E. (2005a). Structural Dynamics – Part 1 - Structural Vibrations. *Delft University of Technology, Faculty of Civil Engineering and Geosciences*.
- Spijkers, J., Vrouwenvelder, A., and Klaver, E. (2005b). Structural Dynamics CT 4140. *Lecture notes*, (January):1–204.

- Sun, X., Huang, D., and Wu, G. (2012). The current state of offshore wind energy technology development. *Energy*, 41(1):298–312.
- Topsector Wind (2018). First offshore wind turbine using the Slip Joint connection successfully installed. <https://www.topsectorenergie.nl/nieuws/first-offshore-wind-turbine-using-slip-joint-connection-successfully-installed>. Accessed on 10.09.2020.
- Tziavos, N. I., Hemida, H., Metje, N., and Baniotopoulos, C. (2016). Grouted connections on offshore wind turbines: a review. *Proceedings of the Institution of Civil Engineers-Engineering and Computational Mechanics*, 169(4):183–195.
- Van der Tempel, J. and Lutje Schipholt, B. (2003). The slip-joint connection, alternative connection between pile and tower. *DOWEC report-F1W2-JvdT-03-093/01-P, Dutch Offshore Wind Energy Converter project*.
- Yoon, G., Kim, S., and Kim, H. (2014). Reliability analysis of monopile for offshore wind foundations using the response surface method. In *New Frontiers in Geotechnical Engineering*, pages 108–117.
- Yuryevich, J. and Wong, K. P. (1999). Evolutionary programming based optimal power flow algorithm. *IEEE transactions on Power Systems*, 14(4):1245–1250.